Thesis for the Degree of Licentiate of Engineering

High temperature corrosion of some selected stainless steels and Ni-base alloys – An advanced microscopy study

Nooshin Mortazavi

Chalmers University of Technology

i

High temperature corrosion of some selected stainless steels and Ni-base alloys – An advanced microscopy study

NOOSHIN MORTAZAVI

Deprtment of Applied Physics
Chalmers University of Technology
SE-412 96 Göteborg
Sweden
Telephone +46 (0) 31- 772 1000
nooshin.mortazavi@chalmers.se

Cover:
The use of TKD and STEM techniques for studying the microstructure of fine-grained oxide scales formed on high-temperature materials. (a) A schematic illustration showing the TKD configuration developed in this project, (b) a STEM micrograph of the oxide scale formed on a FeCrAl stainless steel (alloy Kanthal APMT) exposed to wet environment for 168 h at 1100°C, (c) a TKD map from the boxed area in (b), detection of a nano-sized (~ 30 nm) grain with spinel structure (red) in the scale with otherwise corundum structure (blue).

High temperature corrosion of some selected stainless steels and Ni-base alloys
– An advanced microscopy study

Nooshin Mortazavi
Department of Applied Physics
Chalmers University of Technology

Abstract

The thesis deals with the high temperature corrosion behavior of some selective stainless steels and Ni-base alloys with applications in power generation technologies, *e.g.* boilers fired by biomass and waste. The initial stages of KCl-induced oxidation behavior of two alumina formers (alloys Kanthal APMT and TH1) and one chromia former (alloy Sanicro 25) were analyzed in an O_2/H_2O environment using *in-situ* ESEM method. Besides, the effects of thermal cycling on the oxidation behaviour of a Ni-base alloy HR-214 was studied in air at 1200°C.

The *in-situ* oxidation experiments provided an opportunity to view dynamic processes occurring during the oxidation process ″live″. The *in-situ* results were validated by reference tube furnace exposures. The alloys were corroded in a matter of minutes in the studied environment. The severest corrosion attack occurred locally in the vicinity of KCl particles, where oxide crusts and oxide shells/rims (consisting of Fe-, Cr- and Al-oxides) were formed. STEM studies showed that all the three alloys formed a thin base oxide scale between the KCl particles. Chlorination of the alloys was evidenced by detection of chlorine below the oxide scales.

In the case of the Ni-base alloy HR-214, both isothermal and cyclic exposures led to the formation of a duplex oxide morphology, composed of a columnar alumina layer overlaid by a complex $Ni(Al,Cr)_2O_4$ spinel. The thermal cycling resulted in the formation of vertical cracks in the multi-layered scale. Additionally, STEM/EDX revealed outward transport of Cr through the cracks/alumina grain boundaries, which caused thickening of the outer spinel layer.

Moreover, an attempt was made to develop the newly introduced TKD method to study nano-sized oxide scales. This was conducted by designing a dedicated sample holder, refining the specimen preparation and optimizing the acquisition parameters. These efforts made it possible to achieve data-rich TKD orientation maps (with indexing rates > 85%). The technique was effectively employed to obtain useful information from the microstructure and microtexture of the fine-grained oxide scales. Besides, the technique provided information concerning the crystallographic orientation relationship at oxide/oxide and oxide/alloy interfaces.

Keywords: *high-temperature materials, oxidation, KCl, STEM, STEM/EDX, TKD.*

Acknowledgements

List of Publications

This licentiate thesis is primarily based on the work presented in the following four appended papers and manuscripts. In the text, they are referred by roman numerals.

Paper I

N. Mortazavi, L. Intiso, N. Israelsson, L.-G. Johansson, M. Halvarsson, *In-situ* ESEM investigation of KCl-induced corrosion of a FeCrAl and a model FeNiCrAl alloy in lab air at 450°C. Submitted to *Journal of Electrochemical Society* (2015).

Paper II

N. Mortazavi, L. Intiso, N. Israelsson, L.-G Johansson, M. Halvarsson. *In-situ* investigation of the initial stages of KCl-induced corrosion of a chromia-forming steel at 450ºC using an environmental scanning electron microscope. Submitted to *Corrosion Science* (2015).

Paper III

A. Chyrkin, *N. Mortazavi*, M. Halvarsson, D. Grüner, W.J. Quadakkers. Effect of thermal cycling on protective properties of alumina scale grown on thin Haynes 214 foil. *Corrosion Science* 98 (2015) 688–698

Paper IV

N. Mortazavi, M. Esmaily, M. Halvarsson. The capability of Transmission Kikuchi Diffraction technique for characterizing nano-grained oxide scales formed on a FeCrAl stainless steel. *Materials Letters* 147 (2015) 42-45.

Statement of contribution

My contribution to the papers in the order above;

Paper I: Principal author, analyzing the exposed samples by SEM, SEM/EDX, STEM and STEM/EDX and evaluating the data.

Paper II: Principal author, analyzing the exposed samples by SEM, SEM/EDX, STEM and STEM/EDX and evaluating the data.

Paper III: Performing the STEM, STEM/EDX and the TKD analyses, evaluating the STEM/EDX as well as the TKD data and help with writing of some parts of the paper.

Paper IV: Principal author, producing FIB-prepared thin foils, performing the TKD and STEM analysis and evaluating the data.

Related work

The following papers and manuscripts were also produced during this Ph.D period, but are not included in this thesis;

1. M. Esmaily, *N. Mortazavi*, J.E. Svensson, M. Halvarsson, D.B. Blücher, A.E.W. Jarfors, M. Wessén, L.G. Johansson. Atmospheric Corrosion of Mg Alloy AZ91D Fabricated by a Semi-Solid Casting Technique: The Influence of Microstructure. *Journal of The Electrochemical Society* 162 (2015) C311-C321.

2. K. Hellström, N. Israelsson, *N. Mortazavi*, S. Canovic, M. Halvarsson, J.E. Svensson, L.G. Johansson. Oxidation of a Dispersion-Strengthened Powder Metallurgical FeCrAl Alloy in the Presence of O_2 at 1,100° C: The Influence of Water Vapour. *Oxidation of Metals* 83 (2015) 533-588.

3. M. Esmaily, M. Shahabi-Navid, *N. Mortazavi*, J.E. Svensson, M. Halvarsson, M. Wessén, A.E.W. Jarfors, L.G. Johansson. Microstructural characterization of the Mg–Al alloy AM50 produced by a newly developed rheo-casting process. *Materials Characterization* 95 (2014) 50-64.

4. M. Esmaily, *N. Mortazavi*, M. Shahabi-Navid, J.E. Svensson, L.G. Johansson, M. Halvarsson. On the capability of in-situ exposure in an environmental scanning electron microscope for investigating the atmospheric corrosion of magnesium. *Ultramicroscopy* 153 (2015) 45-54.

5. M. Hörnqvist, *N. Mortazavi*, M. Halvarsson, A. Ruggiero, G. Iannitti, N. Bonora. Deformation and texture evolution of OFHC copper during dynamic tensile extrusion. *Acta Materialia* 89 (2015) 163-180.

6. N. Bonora, G. Testa, A. Ruggiero, G. Iannitti, *N. Mortazavi*, M. Hörnqvist. Numerical Simulation of Dynamic Tensile Extrusion Test of OFHC Copper. *Journal of Dynamic Behavior of Materials* 1 (2015) 136-152.

7. N. Bonora, G. Testa, A. Ruggiero, G. Iannitti, M. Hörnqvist, *N. Mortazavi*. Validating Material Modelling of OFHC Copper Using Dynamic Tensile Extrusion (DTE) Test at Different Impact Velocity. *Bulletin of the American Physical Society* 60 (2015). *In press*.

8. A. Ruggiero, G. Testa, N. Bonora, G. Iannitti, I. Persechino, M. Hörnqvist, *N. Mortazavi*. Deformation and Failure of OFHC Copper Under High Strain Rate Shear Compression. *Bulletin of the American Physical Society* 60 (2015). *In press*.

Preface

The work presented in this Licentiate thesis was performed at the Division of Materials Microstructure, Department of Applied Physics, Chalmers University of Technology, Sweden, in collaboration with the Department of Chemistry and Chemical Engineering (Chalmers) and Forschungszentrum Jülich, Germany. The work was performed under the supervision of Prof. Mats Halvarsson with Prof. Lars-Gunnar Johansson acting as the assistant supervisor. Funding was provided by the Swedish High Temperature Corrosion Center (HTC) and the Swedish Energy Agency.

List of acronyms

BF	Bright Field
BSE	Backscattered Electrons
CBED	Convergent Beam Electron Diffraction
DF	Dark Field
EDX	Energy Dispersive X-ray spectroscopy
EELS	Electron Energy Loss Spectroscopy
EFTEM	Energy Filtered Transmission Electron Microscopy
ESEM	Environmental Scanning Electron Microscopy
ET	Everhart-Thornley
FEG	Field Emission Gun
FIB	Focused Ion Beam
GSED	Gaseous Secondary Electron Detector
HAADF	High-Angle Annular Dark-Field
MAD	Mean Angular Deviation
OAZ	Oxidation Affected Zone
ODS	Oxide Dispersion Strength
PM	Powder Metallurgy
PQ	Pattern Quality
RE	Reactive Element
RSP	Rapidly Solidified Powder
SEM	Scanning Electron Microscopy
SCC	Stress Corrosion Cracking
STEM	Scanning Transmission Electron Microscopy
TACS	Transition from Alumina to Chromia Scaling
TEE	Third-Element Effect
TEM	Transmission Electron Microscopy
TKD	Transmission Kikuchi Diffraction
WD	Working Distance

Table of Contents

1. Introduction

During the last decade, there have been significant attempts to enhance energy efficiency of power plants, which is an important step in the direction of accomplishing the aims of environmental protection and economic growth. Therefore, there has been a strong tendency towards developing materials that can sustain harsh corrosive environments at high temperature in power generation technologies. Boilers fired by biomass and municipal waste, solid oxide fuel cells and heat exchangers are some examples of the technologies concerning production of *green* electricity. The Swedish National Renewable Energy Action Plan (NREAP) has defined a plan; "The overall renewable energy target for Sweden is to have at least a 50% of share of energy generated from renewable sources in gross final energy consumption by 2020". The reports show that Sweden has already exceeded this target by 3% [1].

Despite the significant developments regarding high-temperature materials, there are still needs for further improvements. Fe-Ni-Cr, Fe-Ni-Al and Fe-Ni-Cr-Al are some examples of alloy systems that have been designed to operate in high-temperature corrosive environments in the sectors mentioned above. The ability of all these alloys to resist environments containing corrosive species at high temperatures depends on the formation of protective Cr- and/or Al-rich oxide scales, which should be continuous, strongly bonded to the alloy's surfaces, exhibit acceptable mechanical properties and contain minimum/no amounts of defects and cracks. These requirements should be met in order to be able to effectively employ the alloys in high temperature applications.

To be able to further develop the corrosion resistance of high-temperature materials, it is necessary to understand their oxidation behavior in different corrosive environments by means of various analytical techniques that can analyze and describe them at different length scales, from millimeters to microns to nanometers, and even Ångströms. Such a strategy will result in new findings and open questions that can lead to further developments for producing high-temperature materials with exceptional oxidation resistance.

1.1. Scope of the thesis

The objective of this Licentiate thesis was twofold;

1. Firstly, developing the Transmission Kikuchi Diffraction (TKD) method to analyze fine-grained oxide scales formed on high temperature materials. As indicated above, further improvements in the oxidation resistance of high temperature materials require a precise and more fundamental understanding of the phases formed, crystallographic orientation and size of the grains in the oxide scales. Currently, Transmission Electron Microscopy (TEM) is used to study the structure and chemical composition of grains in the nanoscale. For smaller grains, nano-difraction techniques, such as Convergent Beam Electron Diffraction (CBED) in TEM, are generally used in order to obtain crystallographic information. These TEM-based methods, however, are expensive and time consuming. The TKD method is an Scanning Electron Microscopy (SEM)-based method that is automated (fast) and can provide much useful information regarding the microstructure and microtexture of the oxide scales formed on these materials.

2. Secondly, analyzing and understanding the oxidation behavior of four different types of Fe-base and Ni-base alloys. The alloys tested are materials choices in many high-temperature applications. In this thesis, the initial stages of corrosion of alloys Kanthal APMT, a model alloy named TH1 and Sanicro 25 were studied, as this has an impact on the long-term overall oxidation behavior of these materials. Besides, the effect of thermal cycling on the oxidation behavior of a Ni-base alloy HR-214 was studied using isothermal and cyclic exposures.

The overall goal of this project was to further understand the character of the oxide scales formed on these alloys by means of several high-resolution techniques in order to elucidate the ability of these high-temperature alloys to withstand corrosion in the studied environments.

2. Stainless steels and Ni-base alloys

In high-temperature applications, different types of materials can be used to resist harsh and corrosive environments. Different materials in the form of bulk materials or coatings are utilized depending on the application such as low-alloyed steels, stainless steels, Ni-base alloys, ceramics, etc. A rough estimation of the use of various engineering materials, based on the service temperature, as well as the oxide scale that protects the alloy against oxidation, are provided in **Table 1** [2].

Table 1. Engineering materials used at different temperatures, as well as their protective oxide scale.

Temperature (°C)	Alloy	Protective oxide scale
500	Low alloy steels	$Fe(Fe,Cr)_2O_4$
600	Titanium-base alloys	TiO_2
650	Ferritic stainless steels	Cr_2O_3
850	Austenitic Fe-Ni-Cr alloys	Cr_2O_3
950	Austenitic Ni-Cr alloys	Cr_2O_3
1100	Austenitic Ni-Cr-Al/ Fe-Cr-Al-Y alloys/ (Ni,Fe)CrAlY coatings	Al_2O_3
Above 1100	Ceramics/refractory metals	-

This chapter provides an introduction regarding general high temperature corrosion properties of the materials tested in this project. Two different types (ferritic and austenitic) of stainless steels and two Ni-base alloys were investigated in this project. The commercial names of these high-temperature materials are alloys Kanthal APMT, Sanicro 25, TH1 (model alloy) and Haynes 214.

2.1. Ferritic stainless steels

Ferritic stainless steels are corrosion-resistant iron-based alloys with body-centered cubic (bcc) crystal structure. The main alloying element in these kinds of alloys is chromium (Cr) in the range 10-30 wt.%, depending on the application [3]. From a corrosion point of view, high chromium content is desirable since it promotes the formation of a protective chromia (Cr_2O_3) rich scale.

In order to further increase the corrosion properties, Al can also be added to improve the oxidation properties by the formation of a protective alumina scale instead of chromia scale, especially in higher temperature applications [2], [4], [5].

Ferritic stainless steels are cheaper than austenitic grades since the austenitic stabilizing element, nickel (Ni), is not needed [4]. Moreover, it has been reported that under certain circumstances, *e.g.* in Cl-containing environments, these types of steels exhibit higher corrosion resistance than austenitic stainless steels. They have higher thermal conductivity and a lower thermal expansion compared with their austenitic stainless steels counterparts and are immune to stress corrosion cracking (SCC) [6].

FeCrAl alloys - Kanthal APMT FeCrAl alloys, which are categorized as ferritic stainless steels, usually contain about 15-22 wt.% Cr and 1-5.8 wt.% aluminum (Al). At higher temperatures, typically above 1000°C, they form a protective alumina scale that slows down further oxidation. A sufficient amount of Al, in combination with the high Cr content can result in an increased service life of the components in corrosive environments at temperatures up to 1425ºC. It is known that increasing the Cr content in these alloys decreases the amount of Al required for the formation of the alumina layer, and thus enhances the mechanical properties of the alloys [5], [7] [8]. This is because Cr acts as a secondary getter for oxygen (O), and thus promotes the formation of an external alumina scale at lower Al concentrations [9]. It has been reported that additions of reactive elements (REs) have a positive effect on the high-temperature corrosion behavior of FeCrAl alloys as they increase the adhesion of the developed alumina scale to the alloys' surface [8], [10]. Niobium (Nb), silicon (Si), molybdenum (Mo), and titanium (Ti) are some other commonly used alloying elements in FeCrAl alloys that are also play important roles in the properties of this class of stainless steels. As an example, Mo, which is a ferrite-stabilizing element, is added to improve the hardenability of the steels and also to enhance the high-temperature corrosion properties [10].

This family of stainless steels is a suitable choice for applications with high temperature requirements for heat resistance, such as heating elements in furnaces (see **Fig. 1**) and components in gas turbine engines. Although cast FeCrAl alloys exhibit good oxidation properties, FeCrAl alloys that are fabricated by Powder Metallurgy (PM), in the form of Oxide Dispersion Strength (ODS), or Rapidly Solidified Powder (RSP) metallurgy show good oxidation properties combined with high-temperature strength [8], [11]–[13].

Alloys Kanthal APM, Kanthal APMT (a further development of the alloy Kanthal APM), Kanthal D and Kanthal AF are some example trademarks of this family of stainless steels [3]. Kanthal APMT, which is one of the alloys studied in this project, is a ferritic FeCrAl alloy that contains 21 wt.% Cr, 5 wt.% Al, 3 wt.% Mo and Fe balance with some other minor alloying elements. This alloys has been produced by advanced PM in different forms, such as hot rolled wide plates, bars, rods, wires and extruded tubes. Kanthal APMT is a suitable candidate for a wide range of temperatures and corrosive environments. They are also intended to be employed in components such as retorts and muffles for PM sintering, furnace rollers and furnace furniture where wrought or cast Ni-bas alloys were previously used [14].
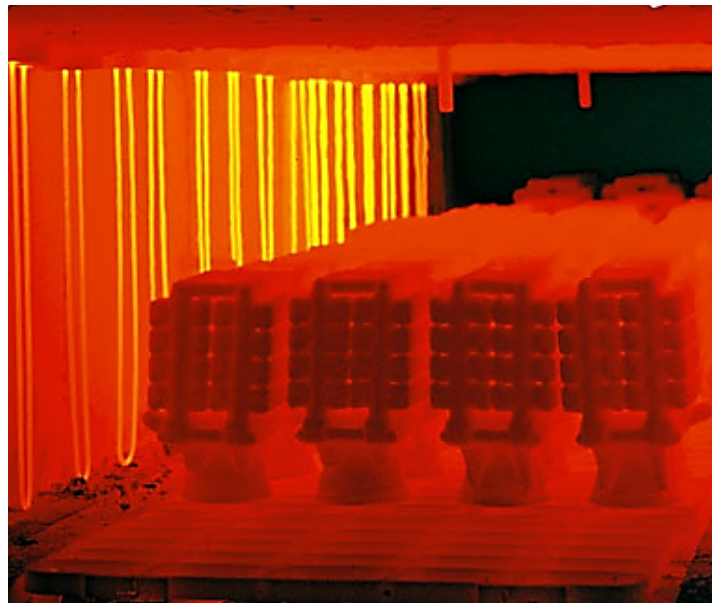
Fig. 1. *The use of Kanthal APMT branded heating wires in electric furnaces [15].*

This relatively new stainless steel has the advantage of withstanding high-temperature oxidation while exhibiting good mechanical strength at high temperatures. The alloy can retain the protective alumina scale up to 1250°C while exhibiting high hot strength. This alloy shows an excellent combination of high corrosion resistance and creep resistance and provides better maximum operating temperature and life in comparison with chromia-forming high-temperature Ni-base alloys that are currently being used in various high-temperature applications. **Figure 2** shows a schematic comparing the high temperature strength and oxidation performance of Kanthal APMT and other stainless steels and Ni-base alloys in oxidizing environments that are currently being used in various high-temperature applications.
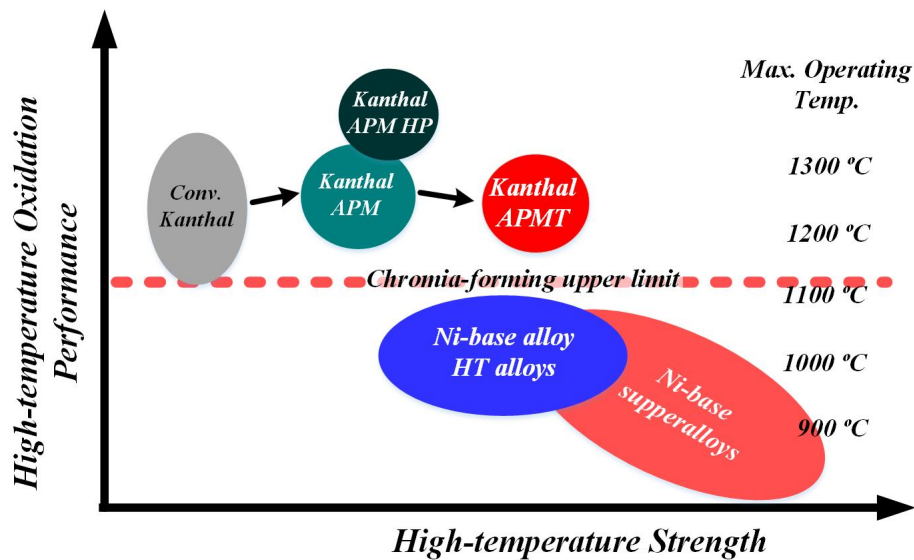
Fig. 2. *Oxidation performance versus high temperature strength for various types of FeCrAl and Ni-base alloys. Reproduced from [14].*

2.2. Austenitic stainless steels

Austenitic stainless steels exhibit excellent corrosion resistance and mechanical properties. Their crystal structure is face-centered cubic (fcc). The Cr content is typically in the range of 16-25 wt.%. Manganese (Mn) and Ni are usually added to stabilize the austenitic structure. They exhibit high ductility and strength, and unlike most of their ferritic counterparts they tend to retain strength at elevated temperatures.

The high-temperature corrosion resistance of austenitic stainless steels relies on the formation of a protective chromium oxide-rich scale. The high temperatures properties of chromia are discussed in the following sections. In these steels, in addition to Ni, which is used to retain the austenitic structure, high Cr content (more than 20 wt.%) is needed to ensure the formation of a protective oxide scale.

It is reported that austenitic stainless steels are less resistant to cyclic exposures than ferritic stainless steels. This is due to the fact that austenitic steels have a higher thermal expansion coefficient than ferritic ones, and thus the formed oxide scale on the surface of austenitic stainless steels is more susceptible to spallation [16]. In order to have austenite as the main phase, there are restrictions on the amounts of Ni, Cr and other alloying elements that are added to the alloy. **Figure 3** shows a Schaeffler diagram that depicts the phase changes in stainless steels according to the Ni and Cr and other alloying elements additions [17].
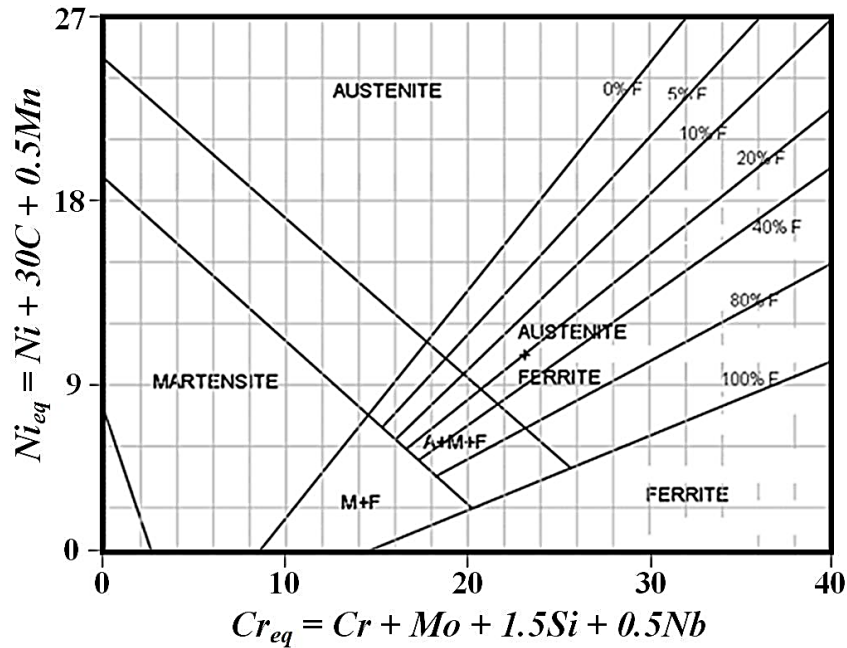
Fig. 3. *Schaeffler diagram showing structure according to the chemical composition of FeCrNi stainless steels. Reproduced from [17].*

FeCrNi alloys - Sanicro 25 Austenitic FeCrNi alloys are used in various heat-resisting applications at moderate to high service temperatures. At high service temperatures and at later stages of oxidation, they may form a layer of poorly protective iron-rich oxide that can deteriorate the oxidation properties of this family of stainless steels [2].

A technological issue for alloys containing high Cr additions is the formation of σ-phase that is a brittle intermetallic compound that degrades the mechanical properties of the alloys. In order to avoid the formation of this phase and effectively stabilize the austenitic structure at room temperature, more Ni or other alloying elements are needed to be added to the alloy [2][18]. In addition to the main constituents, *i.e.* Fe, Cr and Ni, significant amounts of strengthening elements (tungsten (W), cobalt (Co), copper (Cu), and *etc.*) are usually used to improve the formability and mechanical properties, such as creep strength, of the alloys. The applicable temperature range of this grade of stainless steels is up to about 850°C [2].

Sanicro 25 is an austenitic FeCrNi stainless steel with excellent creep strength character in combination with good corrosion resistance at elevated temperatures. The alloy contains 22.5 wt.% Cr, 25 wt.% Ni, balance Fe and lots of other alloying

elements including Cu, W, Co, Mn, Si, Nb, N and C. This alloy is engineered to be used in advanced pulverized coal fired steam boilers in the form of seamless tubes and pipes [19]. The alloy is ideal for reheater and superheater tubes at temperatures up to ~ 700°C. It has been reported that the addition of Si improves the oxidation resistance and promotes the formation of a continuous Cr-rich scale and retards the scale spallation. However, the Si content should be less than 0.3 wt.% in order not to deteriorate the ductility and consequently the alloy's weldability [20], [21].

Cu and W are the main minor alloying constituents in alloy Sanicro 25 with a content of 3 and 3.6 wt.%, respectively. Cu is added to form a Cu-rich phase to improve the creep resistance, see the influence of Cu addition on the creep rupture strength of an 18Cr9NiCuNbN steel in **Fig. 4** [22]. As seen, there is no sufficient increase in creep strength up to about 2 wt.%, however, when Cu content exceeds 2 wt.%, a significant increase in the creep strength is achieved. It should also be noted that a decline in creep rupture ductility occurs when the Cu content exceeds a critical value. Thus the amount of Cu addition is recommended to be kept below 3-4 wt.% [22].
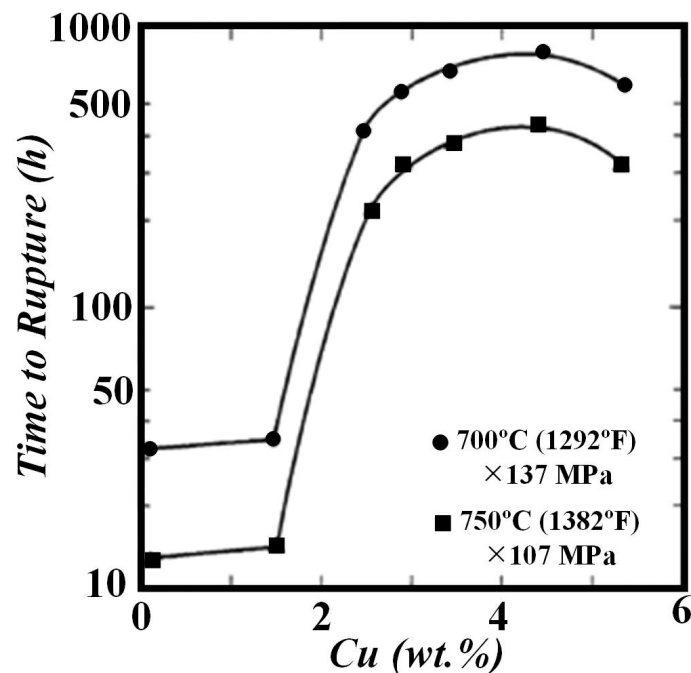
Fig. 4. *Effect of Cu content on creep rupture strength of a18Cr9NiCuNbN steel. Reproduced from [19].*

Another major alloying element, *i.e.* 3.6 wt.% of W, is also added to enhance the high-temperature strength by the aid of solid solution strengthening. However, the W

content should not exceed 4 wt.% in order not to deteriorate the workability of the alloy. As discussed earlier, solid solution hardening and strengthening precipitates, such as (Nb,Cr)N-Z-phase, Cr- and W-rich carbides as well as copper-rich precipitates, provide the high-temperature strength of alloy Sanicro 25 [23]. Additions of Nb and nitrogen (N) are also reported to suppress the carbide precipitation formed on grain boundaries. These alloying elements also contribute to precipitation hardening through the formation of small MX-type nitrides or carbides in the alloy microstructure [24][25].

2.3. Ni-base alloys

Ni-base alloys are widely used in power, chemical and petrochemical industries owing to their high temperature resistance in highly corrosive conditions. They are generally employed as construction materials for components operating at elevated temperatures in oxidizing atmospheres. In these kind of alloys Cr is added to improve the oxidation and sulfidation resistance and also to enhance the strength. During the high temperature exposures/service conditions, a slow growing chromium oxide layer is formed to protect the alloys against oxidation attack [7]. The protectiveness of these alloys against oxidation is therefore depended on the chromium content of the alloy. As is illustrated in **Fig. 5**, the mass gain during oxidation decreases significantly by increasing the Cr content [2]. However, it can be challenging to obtain a single-phase austenitic matrix since Cr is a strong ferrite stabilizers [26], [27].
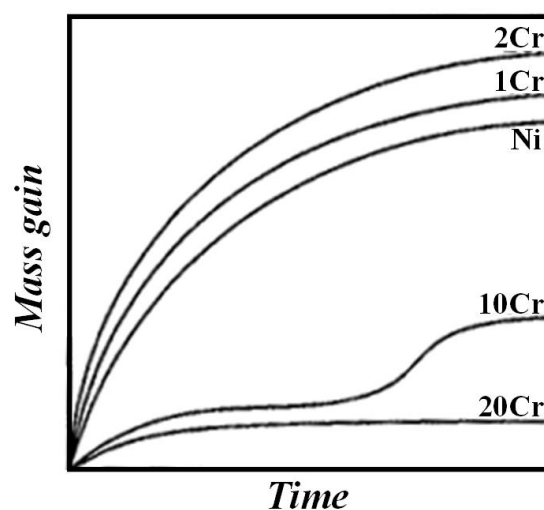
Fig. 5. *Mass change vs. exposure time for different contents of Cr in Ni-based alloys. Reproduced from [2].*

The maximum operating temperature of such alloys is reported to be ~ 1000°C. At higher temperatures, and particularly in water vapor containing atmospheres, a rapid oxidation attack may occur due to the volatilization of the formed chromia layer [28]–[31].

FeNiCrAl alloys - TH1 and Haynes 214 FeNiCrAl alloys, that are a type of Ni-base alloys, contain Al in addition to the other alloying elements in order to form a protective alumina scale at high temperatures. Unlike chromia forming alloys, they do not suffer from chromia evaporation at high temperatures and can be used at temperatures above 1000°C. The added Al forms an intermetallic compound with a chemical composition of Ni_3Al, called gamma prime (γ') in addition to the gamma phase of the substrate. γ' precipitates act as main contributors to strength, especially at higher temperatures. However, it has been reported that γ' precipitates reduce the alloys' ductility, especially at moderate temperatures (≈ 700-740°C). Cr is also used to improve the oxidation resistance of the alloys by facilitating the formation of an adherent slow-growing alumina scale [32]. The wrought nickel-chromium-aluminum-iron alloys usually contain 16-25 wt.% Cr and 2.5-4.5 wt.% Al. They exhibit an excellent resistance to carburization, nitriding and corrosion in chlorine-containing environments and also sufficient creep strength at high temperatures. These alloys are typically manufactured in the forms of bars, ingots, ribbons, wires, shots, sheets and foils [33], [34].

Alloy Haynes 214 is a type of nickel-chromium-aluminum-iron wrought alloy that exhibits very good corrosion resistance at high temperatures, while capable of conventional forming and joining. The application temperature of Haynes 214 is ~ 955°C and above. The oxidation resistance of alloy Haynes 214 relies on the formation of a protective alumina scale. At lower temperatures (below 955°C), a mixture of chromium and aluminum oxide scale forms, which is less protective than the alumina scale, but still comparable to the best nickel-base alloys. Generally, the alloy exhibits good forming and welding characteristics. However, if the alloy is heated in the range of 595-925°C it suffers from strain-age cracking due to the formation of γ'-phase (Ni_3Al). The alloy Haynes 214 is commercially available in the form of plates, sheets, strips, billets, bars and wires, with the typical applications being foil construction honeycomb seals, combustor splash plates in gas turbine

10

industry, catalytic converter internals in the automotive industry, clean firing uses such as mesh belts, trays and fixtures for firing of pottery and fine china, and in the industrial heating market [34].

The effect of different ratios of Ni:Cr:Al:Fe and different types of additives, such as carbide forming (for improving high temperature strength) and REs, on the corrosion behavior of FeNiCrAl alloys have been investigated in the literature[26], [35]–[38]. Studies have shown that they exhibit a good corrosion properties in the temperature range of 600°C to 1300°C [26], [35]–[38]. However, there are still no consistent results regarding the required amount of Al, optimum chemical composition, type and amount of additive elements and grain size of the alloy.

TH1 is a FeNiCrAl model alloy with a nominal chemical composition of 19 wt.% Fe, 18 wt.% Cr, 19 wt.% Fe and Ni in balance, designed and produced by Sandvik Materials Technology. The model alloy has very good high temperature oxidation resistance properties, but lacks the minor alloying additives that are required for high temperature strength. REs are also present in its chemical composition to increase the oxide properties and the alumina scale adhesion [35], [39], [40].

3. High temperature oxidation theory

Most metals and alloys have the inherent tendency to revert from a processed metallic state to their more natural ore state. Hence, various types of oxide, nitrides, sulphides and chlorides may form depending on the environment that metallic materials are being exposed to. The oxidation of metals at ambient temperature is very little since the reaction rates are slow. At high temperatures, however, the rate of oxidation increases rapidly and become a rather costly and problematic process. For instance, direct annual cost of corrosion in the United States is reported to be $276 billion while neglecting many other indirect costs (around 3.1 % of the nation's gross domestic product) [41]. These types of data show the serious challenges that corrosion presents to equipment and components made of metallic materials.

In general, the corrosion resistance of Fe-base and Ni-base alloys relies on the protective character of the oxide scale formed on their surface while they are exposed to corrosive environments. This chapter of the thesis provides the basics of oxidation as well as some information concerning the current theories of oxidation at elevated temperatures.

3.1. Oxide formation and thermodynamics

The following well-known equations express the oxidation reaction of a metal (M) in the presence of oxygen or water vapor;

$$xM + \frac{1}{2}yO_2 = M_xO_y \tag{1}$$

$$xM + yH_2O = M_xO_y + yH_2 \tag{2}$$

According to the second law of thermodynamics, at constant temperature and pressure, the occurrence of the reaction depends on the change in Gibbs free energy (G') of the system, which is described by equation (3);

$$G' = H' - TS' \tag{3}$$

where H' and S' are the enthalpy and entropy of the system and T is the temperature. If the free-energy change ($\Delta G'$) is negative then a spontaneous reaction is expected, if

$\Delta G'$ is positive then the process is thermodynamically impossible and finally if $\Delta G = 0$ equilibrium condition is expected.

For a typical chemical reaction of aA + bB = cC+ dD, ΔG' can also be expressed as in the following equation:

$$\Delta G' = \Delta G° + RTln(\frac{a_C^c a_D^d}{a_A^a a_B^b})$$
(4)

where $\Delta G°$ is the standard Gibbs free-energy change, R is the gas constant, T is the temperature and a is the thermodynamic activity of the products and reactants and is described according to equation (5):

$$a_i = \frac{p_i}{p_i°}$$
(5)

where P_i stands for the partial pressure of a gaseous species and $P_i°$ is the same quantity but corresponding to the standard state of i. When the reaction is in the equilibrium form, *i.e.* ΔG' = 0, equation (4) reduces to the following equation:

$$\Delta G° = -RTln(\frac{a_C^c a_D^d}{a_A^a a_B^b})_{eq} = -RTln(K)$$
(6)

where K is the equilibrium constant. In selective oxidation of alloys it is important to determine the condition for the formation of each corrosion product. A convenient way is to use Ellingham diagrams for oxides in which the standard free energy of oxide formation (ΔG°) versus temperature for different compounds is plotted. **Figure 6** shows the Ellingham diagrams for simple oxides. In the diagram, the lower the position of the line the higher the stability of the oxide. These diagrams allow the comparison of the relative stabilities of different oxides; for instance, it shows that the affinity of Cr and Al for oxygen is greater than that of the Ni and Fe. Besides, the diagram shows that the formation of Cr_2O_3 is thermodynamically more favorable than the formation of Fe_2O_3 when a FeCr alloy is oxidized, if there is sufficient amount of Cr in the alloy. Additionally, the partial pressure of oxygen at which the metal and oxide coexist can be obtained from the diagram. This can be done by sketching a straight line from point O through the free energy line at the desired temperature and reading the oxygen partial pressure (pO_2) [2], [42].
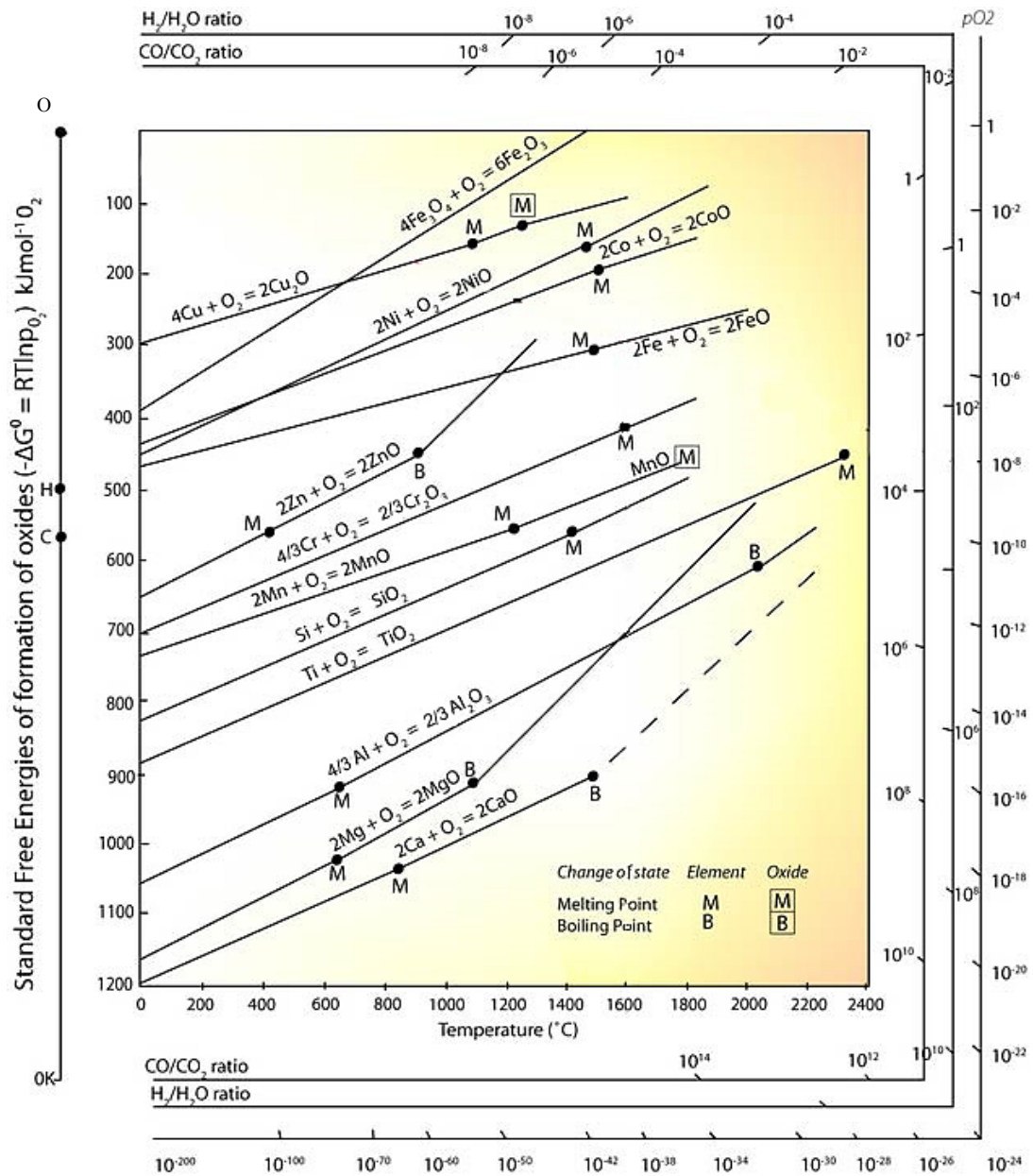
Fig. 6. *The Ellingham diagram for selected oxides showing the temperature dependence of the stability for compounds [2].*

3.2. Diffusion through defects

When an oxidation reaction has occurred, the solid reaction product (MO) will form and separate the metal from the gas. In order for the reaction to proceed, ions and/or electrons of the reactants need to diffuse through the formed solid oxide layer, *i.e.* solid-state diffusion must occur. Diffusion of the ions/electrons is often assisted by defects, which are an inherent part of most of the crystalline materials. There are different types of defects in the scale.

In stoichiometric crystals, which have a low concentration of defects, like Al_2O_3 or SiO_2, the predominant defects are Schottky and Frenkel defects [14]. However, most of the formed oxides, especially the transition metal oxides, are non-stoichiometric compounds, which exhibit higher concentration of defects compared to stoichiometric oxides due to the multiple oxidation state of the metal ions. These oxides are electrically neutral but there is always an excess or deficit of ions, which is compensated by electron vacancies or excess. They are classified as negative (n-type) or positive (p-type) semiconductors. Negative semiconductors (n-type) are the oxides with metal excess or deficit oxygen ($M_{1+x}O$ or MO_{1-x}), while positive semiconductors (p-type) are the oxides with metal deficit or excess oxygen ($M_{1-x}O$ or MO_{1+x}). **Figure 7** summarizes the different solid-state transport processes in non-stoichiometric oxides. As can be seen, when the scale growth is due to cation migration it would occur at the scale-gas interface, and therefore the scale grows outwards. Whereas, when the scale grows by anion migration, the scale formation would be at the metal-scale interface and consequently inward oxide scale growth will occur.

In addition to the bulk diffusion through the oxide scale, which is governed by concentration of interstitials and vacancies and are zero dimensional defects, there are other types of defects including one dimensional defects, such as dislocations, two dimensional like grain boundaries and finally three dimensional defects such as second phase precipitates.
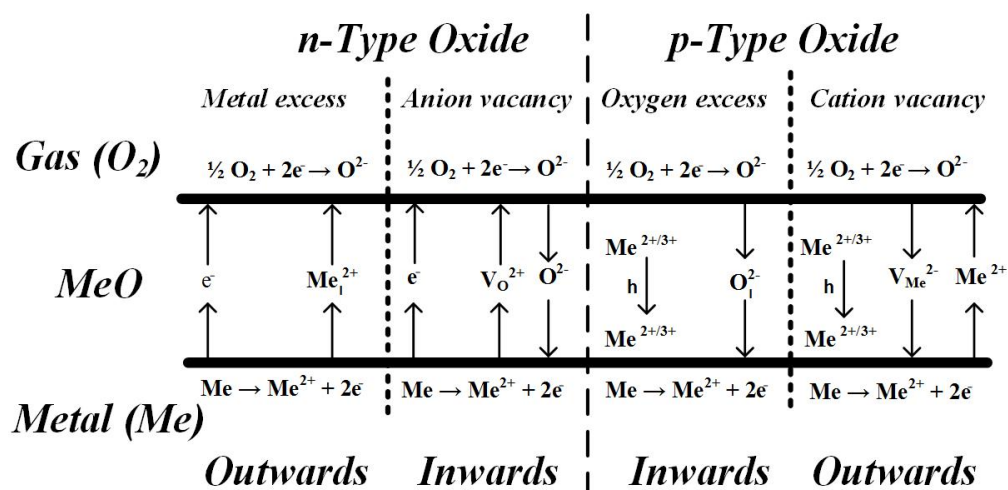
Fig. 7. Summary of solid-state transport process in different types of non-stoichiometric oxides and the growth directions. Reproduced from [43].

16

As an example, the diffusion coefficient of Ni in a polycrystalline NiO lattice, along dislocations and grain boundaries at different temperatures are shown in **Fig. 8**. As seen, grain boundaries and dislocation diffusion are the dominant diffusion mechanisms. It may be noted that the contribution of lattice diffusion is increased at higher temperatures [44].
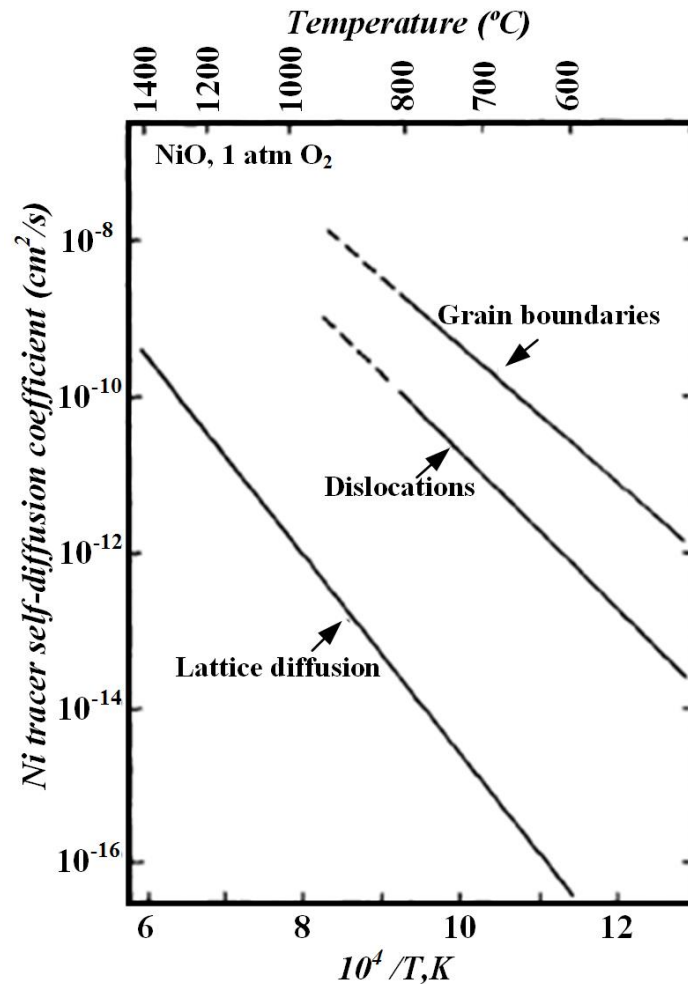
Fig. 8. *Diffusion coefficient vs. temperature for Ni in the lattice, along dislocations and along grain boundaries in polycrystalline NiO. Reproduced from [44].*

3.3. Kinetics of oxidation

To analyze the oxidation rates, it is a common approach to investigate the scale growth as a function of time. For this aim, mass gain, which is proportional to the oxide thickness, is plotted against the exposure time. For many metals and alloys, where the oxide layer is relatively uniform and the scale volatilization is small, three kinetic laws, namely linear, parabolic and logarithmic, describe the oxidation rate. These three kinetic laws are schematically shown in **Fig. 9**.
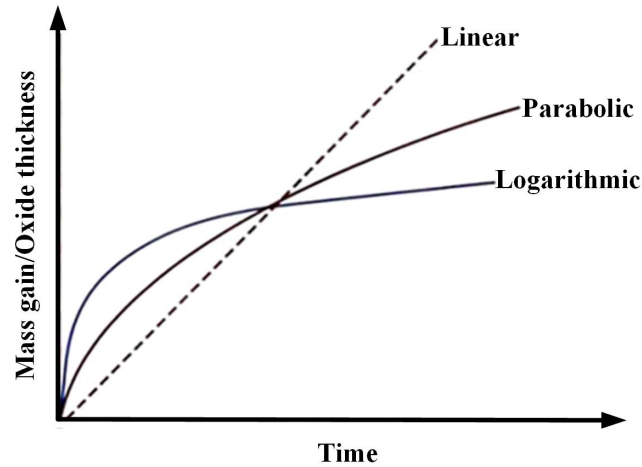
Fig. 9. Mass gain or oxide thickness versus time showing the linear, parabolic and logarithmic kinetics laws for metal oxidation [45].

It should be mentioned that these kinetic laws are derived from limiting and ideal cases. Under certain conditions, the kinetic behavior of an oxidation process exhibits one of these three oxidation rates. However, generally the kinetic behavior is much more complicated.

Linear rate law The linear kinetic law is observed when the oxidation proceeds at a constant rate and is expressed by the following equation:

$$x = k_l t + C \tag{7}$$

where x is the oxide thickness, t is the time, k_l is linear rate constant and C is thickness at $t = 0$. Linear growth is common when a surface reaction, rather than transport through the scale, governs the oxidation rate. It is typical for metals with porous or cracked oxide films where the transport of reactants are equal or faster than the chemical reaction and the oxide scale is not protective, for example tantalum (Ta) oxidation. It's also common for the initial stages of oxidation where the formed oxide layer is too thin to protect the alloy underneath.

Parabolic rate law The oxidation rate of many metals and alloys at elevated temperatures follows the parabolic rate law according to equation (8):

$$x^2 = k_p t + C \tag{8}$$

18

where k_p is the parabolic rate constant, t stands for the time, and C is the thickness at $t = 0$. Here, the transport of ionic species or electrons through the oxide scale is the rate controlling process. Accordingly, the rate of oxidation slowly decreases as the scale thickens. Parabolic behavior is typical for metals with thick coherent oxides, for example Cu and Fe [3].

Logarithmic rate law The logarithmic law is mostly applicable at low temperatures, where the oxidation rate is inversely proportional to time. This type of oxidation kinetic is seen in metals like Fe, Cu and Al. Logarithmic behavior is described by the following equation:

$$x = k_{log} \log(at + 1) \tag{9}$$

where k_{log} is the logarithmic rate constant and a is a dimensional factor. During logarithmic growth, the oxidation is fast in the beginning and then slowed down to a very low value, which is the most desirable type of oxidation rate. In the logarithmic rate behavior, the rate of reaction is likely to be controlled by the transport of electrons/ions from the alloy substrate through the oxide scale(s) to the adsorbed oxygen atoms at the specimen surface. Other mechanisms have also been proposed to be responsible for logarithmic oxidation behavior, such as cavity formation in the oxide film, see for example [2], [5], [45].

Breakaway oxidation This case of oxidation (breakaway or rapid non-protective oxidation) occurs when an originally protective oxide scale abruptly fails to protect the alloy against oxidation. The reasons can be due to the changes in the chemical composition of the alloy or oxide or mechanical failure of the scale [3], see below.

3.4. Mechanical properties of the oxide scale

The protective character of the oxide scale may be deteriorated due to internal or external stresses. Such stresses are known to result in cracking or spallation. Hence, the mechanical properties of the scale play a crucial role in protection, especially at elevated temperatures where thermal and mechanical stresses are unavoidable.

During cyclic oxidation, where considerable thermal stresses are present, significant mass losses may be observed due to oxide scale spallation. Besides, the differences in

thermal expansion coefficient of the scale and the metal substrate are reported to deteriorate the mechanical properties of oxide scales in thermal cycling [3].

The mechanical properties of the scale can be deteriorated in different ways. For instance, outward diffusion of cations, in combination with inward diffusion of vacancies, can produce subsurface vacancies. At the later stages of oxidation, the coalescence of voids may cause cracking at the oxide scale. Additionally, as the oxide scale grows the volume difference between the metal substrate and the oxide may cause stresses at the interface. This is expected to decrease the adherence of the scale and lead to the mechanical failure of the scale. Stresses can be relieved by different mechanisms, such as plastic deformation of the metal or cracking of the oxide layer. Generally, the scale deforms and buckles at lower stresses, while at higher stress levels detachment of the scale occurs [5].

Therefore, not only the formation of a protective scale, which can block the flux of ionic species and act as a barrier against aggressive species, is important, but also it is essential that the scale maintains its mechanical properties during the service conditions and does not lose its adherence to the metal substrate [5], [46].

4. High temperature corrosion of stainless steels and Ni base alloys

During high temperature exposures, different oxides or other compounds may form depending on the temperature, environment, alloying elements and time of exposure. In the following sections the properties of common oxide scales that may form on stainless steels and Ni base alloys are discussed.

4.1. Iron oxides

The three different kinds of iron oxides that may form during high temperature oxidation process are wüstite (Feo), magnetite (Fe_3O_4) and hematite (Fe_2O_3) [2]. These oxides grow through the outward diffusion of Fe. A multilayer oxide is usually developed during high temperature oxidation [14]. Due to the higher partial pressure of oxygen needed for the formation of hematite in comparison with other types of iron oxides, it forms as the outermost layer (gas/oxide interface) while wüstite is formed at the oxide/metal interface, which is in accordance with the decrease in the oxygen partial pressure in the innermost part of the oxide layer [3].

Wüstite can form at temperatures higher than 570°C and is a p-type non-stoichiometric oxide, see **Fig. 11**. Thus, due to the very high concentration of cationic vacancies, the mobility of cations and electrons is high. As a result, the growth rate is very fast, and hence this layer is expected to form the thickest layer among the three Fe oxide types. Accordingly, the oxide is characterized as a non-protective oxide scale [2], [5].

Magnetite with an inverse spinel crystal structure contains both Fe^{3+} and Fe^{2+} ions in its crystal structure. Its structure is close to stoichiometric and behaves as an n-type oxide. The oxide is more corrosion resistant than wüstite. It is known that the stability of magnetite increases with increasing temperature [5].

Hematite has a corundum structure and is classified as an n-type semiconductor at temperatures in the range of 650-800°C and a p-type semiconductor at higher temperatures. Since hematite contains both ionic oxygen vacancies and metal interstitials both outward and inward scale growth is possible. It is worth mentioning that hematite is the most protective iron oxide [5], [47].

21
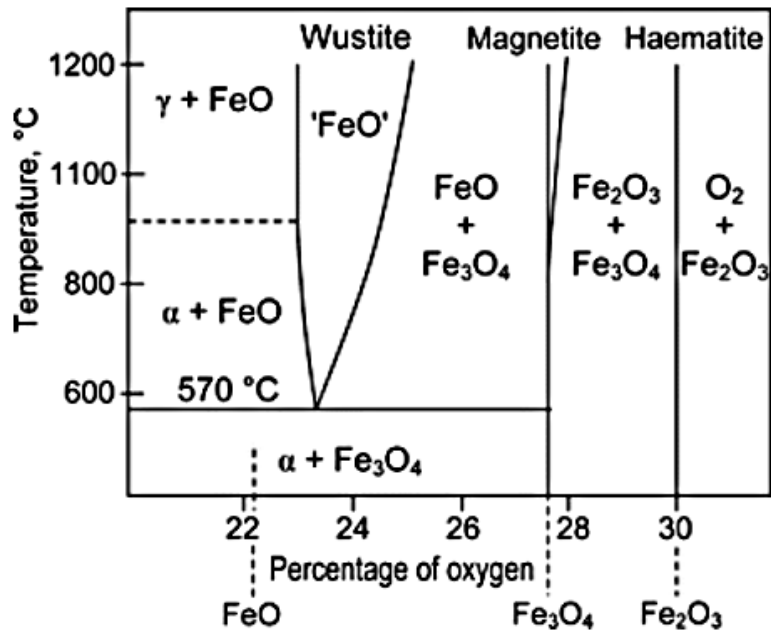
Fig. 11. *The iron-oxygen phase diagram (wt.%) [2].*

4.2. Chromium oxide

At temperatures < 900ºC, Cr develops a protective chromium oxide, eskolaite (Cr_2O_3), which is also called chromia. This oxide exhibits a better protective character than any of the iron oxides, and thus, it is commonly used to enhance the high-temperature oxidation resistance of Fe- and Ni-base alloys. The oxide has a corundum crystal structure with a very low level of non-stoichiometry. It is a p-type semiconductor with cation vacancies dominating [48]. Scale growth is reported to mostly occur by outward migration of Cr ions along the grain boundaries [49].

The oxide developed on Fe-Cr alloys is always a mixed solid solution of Fe and Cr since both ions have similar sizes, see the Fe-Cr-O phase diagram shown in **Fig. 12**. The protective character of the oxide depends on the Cr content in the oxide. Generally, by increasing the Cr content the oxidation resistance of the alloys increases. However, the protective character of pure chromia is lower than the mixture of chromia with a small substitution of Fe. This is because the existence of Fe^{2+} ions reduces the cation vacancies and consequently suppresses the ionic conductivity of the protective scale.

It's worth mentioning that the Fe-Cr system is not a good candidate for use in high temperature applications with long-term exposures because of the wide range of solid

22

solutions formed by the Fe_2O_3-Cr_2O_3 rhombohedral oxides. Even at higher Cr contents, Fe ions are dissolved in the chromia scale and form an outer layer of fairly pure Fe oxide. Higher content of Cr (higher than 20-25 wt.%) is not applicable without using other alloying elements due to the formation of sigma-phase that will cause the embrittlement of the alloy [2].
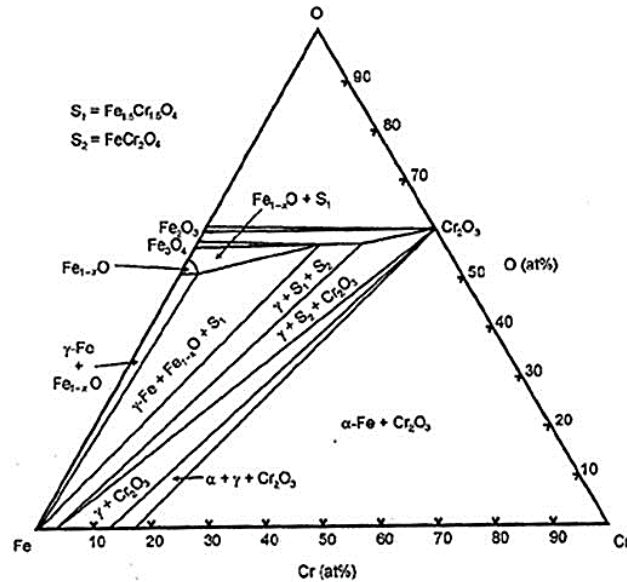
Fig. 12. *Isothermal section of the Fe-Cr-O phase diagram at 1200°C [2].*

Additionally, chromia may be evaporated and consumed in the presence of water vapor and/or oxygen and form chromic acid [50]–[52], and in the presence of alkali salts it may form alkali chromate [53]–[56]. It is known that chromia is consumed according to the following equations;

Cr_2O_3 *(s)* + 3/2 O_2 *(g)* → 2CrO_3 *(g)*   (10)

1/2Cr_2O_3 *(s)* + 3/4 O_2 *(g)* + H_2O *(g)* → $CrO_2(OH)_2$ *(g)*   (11)
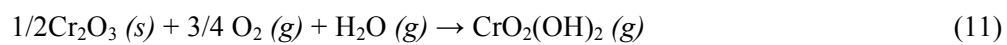
The occurrence of such reactions removes the chromia from the surface of the alloy and consequently causes severe corrosion attacks to the subjacent metal substrate [2].

4.3. Aluminum oxide

Aluminum oxide, also called alumina, has many polymorphs with the chemical composition Al_2O_3. The formation of different forms of alumina, such as γ-Al_2O_3 (face centered cubic), δ-Al_2O_3 (tetragonal), θ-Al_2O_3 (monoclinic), κ-Al_2O_3 (orthorhombic), and α-Al_2O_3 (rhombohedral) depends on environmental factors, such as temperature, as well as on the chemical composition of the substrate that the alumina grows on. All the forms are considered as a non-protective oxide scale and are thermodynamically metastable, except α-alumina. Transient forms of alumina, i.e. (α, χ, η, δ, κ, θ, γ, ρ), are considered to form more extensively at temperatures < 1000°C and especially during the initial stages of oxidation. The most thermodynamically stable form of Al oxide, i.e. α-alumina, is highly stoichiometric and usually tends to form at higher temperatures and longer exposure times [7]. The crystal structure of α-Al_2O_3, which is called corundum structure, ideally comprises close packed planes (A and B planes) of large oxygen anions and smaller Al ions on octahedral interstices (a, b or c), as depicted in **Fig. 13**. Due to its highly stoichiometric structure, the oxidation rate is very low. α-Al_2O_3 generally has a high scale adherence to the metal substrate and unlike chromia it exhibits an excellent chemical stability towards water.
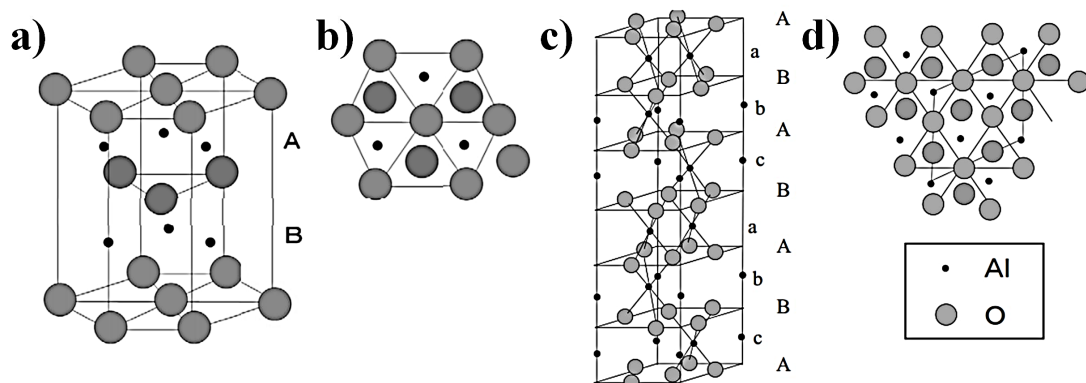
Fig. 13. (a) The structure of α-alumina, (b) top-view of (a), (c) and (d) the complete stacking sequence and its top-view of O and Al layers that form A-a-B-b-A-c-B-a-A-b-B-c-A... [57].

The growth of α-alumina is mostly inward, primarily by diffusion of oxygen ions along the oxide grain boundaries. Transient oxides, such as chromia and iron oxides with corundum crystal structure, can act as a nucleation sites for the formation of α-Al_2O_3, for instance during the oxidation of FeCrAl alloys and facilitate the formation of protective α-alumina.

The main drawback of α-Al$_2$O$_3$ is its vulnerability to crack formation and spallation. This occurs because of the differences in thermal expansion coefficients between α-Al$_2$O$_3$, which is low, and the substrate. Thus, compressive stresses may arise during temperature changes. Furthermore, growth stresses or stresses that are applied in service conditions may lead to scale failure as well.

Additionally, the transformation of metastable types of alumina to α-Al$_2$O$_3$ is frequently associated by volume changes (around 14 %) and may give rise to void formation within the protective scale [8]. There has been extensive research devoted to improving the mechanical properties of the alumina scale, such as adding small amounts of REs [10], [58]–[60].

The addition of REs has several beneficial effects on the corrosion behavior of alumina forming alloys. It is suggested that they promote selective oxidation by reducing the necessary amount of Al for the formation of a protective alumina scale. Besides, REs may reduce the growth rate of alumina by reducing the outward diffusion of Al ions towards the alumina scale. Additionally, it is reported that REs increase the scale adhesion by binding elements such as sulfur and thus preventing it from segregating at the scale/alloy interface, and also by decreasing the void formation at the interface [59].

4.4. Mixed spinel-type oxides

Mixed oxides with a spinel crystal structure such as (Fe, Cr, Ni)$_3$O$_4$ may additionally form on the surface of Fe-base alloys that contain alloying elements, such as Ni and Cr. The mixed oxides may also develop on Ni-base alloys containing Cr and Al. Because of the approximately same ionic size of Fe, Cr and Ni, it is possible to form different combinations of oxides depending on the composition of the alloy and also the oxygen partial pressure in the scale [5]. These oxides are considered non-protective in high-temperature applications.

4.5. Effect of O$_2$ and H$_2$O

Generally, it is reported that water vapor increases the oxidation rate of both alumina and chromia forming alloys due to the enhancement of ion diffusion through the oxide scale [61]–[63]. The effect of water vapor and oxygen is even more pronounced in chromia forming alloys since it reacts with the protective chromia scale and forms volatiles species such as $CrO_3(g)$, $Cr_2O_2OH(g)$, $Cr_2O_2(OH)_2(g)$ [50], [64].

For instance, Asteman *et al.* [50] has suggested that in the presence of water vapor on a 304L stainless steel at 600°C the chromia scale deteriorated and chromic acid formed:

$$1/2 Cr_2O_3\ (s) + 3/4\ O_2\ (g) + H_2O\ (g) \rightarrow CrO_2(OH)_2\ (g) \qquad (11)$$
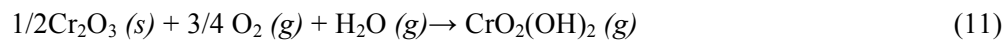
In another study done by Liu *et al.* [65] on a FeCrAlRE alumina forming alloy, it is reported that the presence of water vapor hindered the phase transformation from γ-Al$_2$O$_3$ to α-Al$_2$O$_3$ which resulted in an increased mass gain.

4.6. KCl-induced high temperature corrosion

In addition to oxygen, corrosive species such as H_2O, HCl, SO_2, CO_2, *etc.* can be present, for instance in the fireside environment of waste and biomass fired boilers. Among them chloride-containing compounds like KCl, $NaCl$, HCl and Cl_2 are considered to be the most corrosive species. Their corrosivity towards high-temperature alloys is well-documented in the literature [66], [67].

There has been large number of studies regarding the effect of chloride-containing compounds on the corrosion behavior of alloys, see for instance references [68]–[73]. In most of the cases the corrosive effect of chlorine has been explained by a well-known mechanism named "activation oxidation" or "chlorine cycle" [5].

4.6.1. Active oxidation or chlorine cycle

Active oxidation of alloys usually happens when the oxide scale exhibits a poor protectiveness and chloride-based species significantly speed up the rate of corrosion [74]. According to this mechanism, chlorine may be present initially or formed by the

oxidation of HCl and/or by the reaction of condensed chlorides, such as KCl or NaCl, with the oxide scale according to the following type of reactions:

$$2HCl + \frac{1}{2}O_2 = Cl_2 + H_2O \tag{11}$$

$$2KCl + Cr_2O_3 + \frac{1}{2}O_2 = K_2Cr_2O_4 + Cl_2 \tag{12}$$

If chlorine penetrates through the oxide scale to the metal/oxide interface, metal chlorides such as CrCl$_2$ and FeCl$_2$ are able to form according to reaction (13):

$$\frac{x}{2}Cl_2(g) + M(s) = MCl_x(s) \tag{13}$$

Usually, the metal chlorides have high vapor pressure at elevated temperatures (around 500°C), and thus may volatilize. The volatilized transition metal chloride can diffuse outwards through the cracks and pores of the oxide scale to where it encounter higher oxygen partial pressures and decomposes to a porous oxide layer and also releases chlorine:

$$yMCl_x(g) + \frac{z}{2}O_2 = M_yO_z(s) + \frac{xy}{2}Cl_2(g) \tag{14}$$

The formed chlorine can diffuse back towards the oxide/metal interface and start a new cycle, the chlorine cycle, and sustain the oxidation process [71], [74].

4.6.2. Effect of potassium ions in the breakdown of the scale

As discussed earlier, the protective character of the mixed chromium iron oxide scale depends on the Cr content of the scale. Hence, any reaction that depletes Cr in the oxide can deteriorate the corrosion properties. In this regard, potassium cations can be corrosive toward stainless steels or Ni-base alloys protected by a chromium-rich oxide as it reacts with the chromia scale to produce potassium chromate according to reaction (15):

$$\frac{1}{2}Cr_2O_3(s) + \frac{3}{4}O_2(g) + H_2O(g) + 2KCl = K_2CrO_4(s) + 2HCl(g) \tag{15}$$
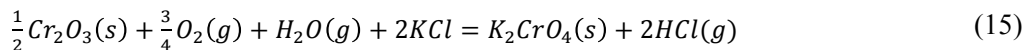
As a result, the Cr content is lowered in the Fe-Cr oxide scale, and an iron-rich and non-protective oxide scale remains [53], [54], [70], [75]–[77].

4.6.3. Corrosion by molten phases

Chlorides are usually present in molten species formed on the surface of alloys at elevated temperatures. These species are present in waste-fired boilers and cause increased corrosion rates [66], [78]–[80] because of the fast kinetics of reactions in the liquid phase and consequently more rapid transportation of ionic species [5]. It is known that the melting point of most alkali species and transition metal chlorides are higher than typical superheater temperatures. However, when these species are in contact with other compounds existing in the deposits, low-melting eutectic mixtures are developed. For instance, while the melting temperature of KCl is reported to be 772°C, the eutectic mixture of KCl and metallic chlorides is much lower, reaching to a value of ~ 355°C for KCl-FeCl$_2$ systems [61]-[63].

5. Experimental procedure

5.1. Test materials

The materials tested in this project are two high-alloyed stainless steels; a FeCrNi alloy and a FeCrAl alloy with the commercial names of Sanicro 25 and Kanthal APMT, respectively. Besides, two Ni-base alloys with the model name of TH1 and commercial name of HAYNES 214 alloy (HR-214) were studied. Alloys Sanicro 25, TH1 and APMT were supplied by Sandvik Heating Technology, Sweden, and HR-214 was delivered from Haynes International, Germany. The chemical compositions, in weight percent, of these materials are listed in **Table 2**.

Table. 2. *Chemical composition (in wt.%) of the stainless steels and Ni-base alloys used in this project. Note: Alloys APMT and TH1 have traces of rare elements (hafnium (Hf), zirconium (Zr) and yttrium (Y)).*

Alloy	Fe	Cr	Ni	Al	Mn	Mo	Si	Nb	C	Cu	W	Co	N
San 25	*Bal.*	22.6	25.5	-	0.5	-	0.25	0.44	0.08	2.99	3.45	1.57	0.24
APMT	*Bal.*	21	-	5.0	≤0.4	3.0	≤ 0.7	-	≤ 0.008	-	-	-	-
TH1	19.6	18.2	*Bal.*	4.5	-	-	-	-	-	-	-	-	-
HR-214	3.6	16.0	*Bal.*	4.4	0.17	-	0.26	-	-	-	-	-	-

In paper (I) and (II) all the samples were KCl contaminated while in paper (III) and (IV) no KCl salt were used.

5.2. Furnace exposures

Furnace exposures of alloys APMT (paper I and IV), TH1 (paper I) and Sanicro 25 (paper II) were carried out using a horizontal silica tube furnace by the help of our co-workers at the Department of Chemistry and Chemical Engineering at Chalmers University of Technology. The isothermal exposures were performed at 450°C for 1 hour with a net flow rate of 200 ml/min (0.2 cm/s) in laboratory air. In paper (I), for the case of alloy APMT, the alloy was exposed either in dry atmosphere containing 5 vol.% O_2 + 95 vol.% N_2 or in wet oxidizing atmosphere containing 5 vol.% O_2 + 55 vol.% N_2 + 40 vol.% H_2O for 24 and 168 h at 1100 °C.

For the case of alloy HR-214 (paper III), isothermal and cyclic oxidation experiments were performed in a horizontal resistance-heated furnace by our co-workers at Forschungszentrum Jülich, Germany. The heating and cooling rates were ~10 K min^{-1}. Exposures were done in static laboratory air at 1200°C. The cyclic exposures

29

were interrupted every 100 h for weight measurements, see [81]. At each time interval, one sample was removed from the furnace for microstructural analyses. The longest exposure time during the thermal cycling was 600 h, *i.e.* 6 cycles. The isothermal tests were run separately for 300, 500 and 720 h, respectively, without intermediate weight measurements.

5.3. Scanning Electron Microscopy (SEM)-Energy Dispersive X-ray spectroscopy (EDX)

The Scanning Electron Microscope (SEM) employs an electron gun that shoots electrons with high kinetic energy (~10 keV) to a surface of a solid bulk specimen. Interactions between the specimen and electrons result in a variety of signals that are emitted from different penetration depths [82], [83], see the schematic illustration in **Fig. 14**. Useful information from the specimen can be achieved by detecting the scattered electrons and X-rays that are ejected from the target surface [84]. A common application of the SEM is the imaging of topography (shape, size, surface texture) of 3-Dimensional (3-D) objects, see for example the Secondary Electron (SE) micrograph in **Fig. 14** [83], [84]. Low-energy SEs give rise to such topographical contrast. SEs are generated from a relatively small interaction volume, in the order of tens of nanometer, around the spot where the electrons hit the specimen surface.

BackScattered Electrons (BSEs), however, are generated from larger volumes, in the order of several hundreds of nanometer. They have higher energies than SEs and result in compositional contrasts, and therefore some qualitative elemental information can be obtained [83]. Thus, areas of high average atomic number (Z) will appear brighter with respect to areas of low Z. It should also be mentioned that the excitation volume depends upon several parameters, such as the energy of primary electrons, i.e. accelerating voltage (E_0), and the average Z value of the sample being studied in the SEM, see **Fig. 15a** [85].

The volume of electron interaction with respect to these parameters can be modeled by means of the Monte Carlo method, see **Fig. 15b**. As seen in **Fig. 15**, the resulting excitation volume can have a hemispherical (for materials with high Z, like gold) to jug-like (for material with relatively low Z, like aluminum) shape with the neck of the jug at the location where the electrons hit the sample surface (**Fig. 15a**). Monte Carlo

30

simulations can also be used to show the strong effect of Z and density of the sample on the interaction depth, see **Fig. 15b** [86], [87].
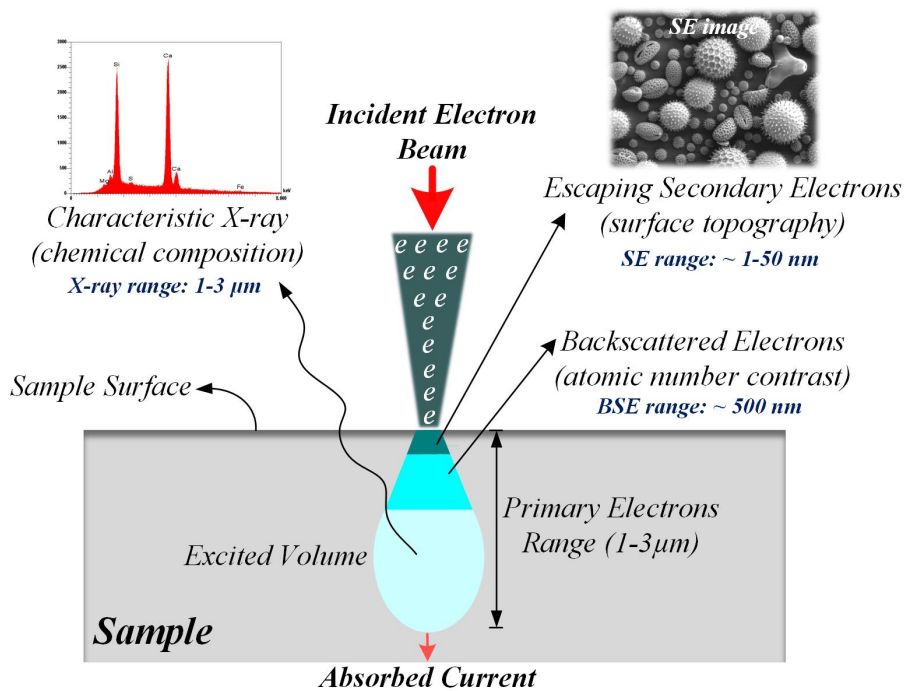
Fig. 14. *Illustration image showing the SE, BSE and X-ray signals that derive from electron beam/sample interactions in the SEM. Some typical values are given. Reproduced from* [83], [88].

In addition to SE and BSE imaging, SEM provides the opportunity to determine the chemical composition of selected points on the specimen surface using Energy Dispersive X-ray spectroscopy (EDX), also known as EDS. As shown in **Fig. 14**, X-rays are emitted from deeper parts of the excited volume as compared to SEs and BSEs. This method is considered as a fairly fast, inexpensive, and basically non-destructive analytical technique [89].

In the present project, SEM was widely used to study the morphology and chemical composition of corrosion products using an FEI Quanta 200 Environmental Scanning Electron Microscopy (ESEM) with a Schottky Field Emission Gun (FEG), and a Zeiss Ultra 55 FEG SEM. Both instruments are equipped with Oxford Inca EDX systems. SE and BSE imaging were done with a range of acceleration voltages from 10 to 20 kV. SEM/EDX was also used for local chemical analysis as well as elemental mapping of the corroded sample surfaces. A pre-tilted (45º tilt) sample holder was used for SEM imaging and EDX analyses on the cross sections made by the Focus Ion Beam (FIB) milling procedure, see below.
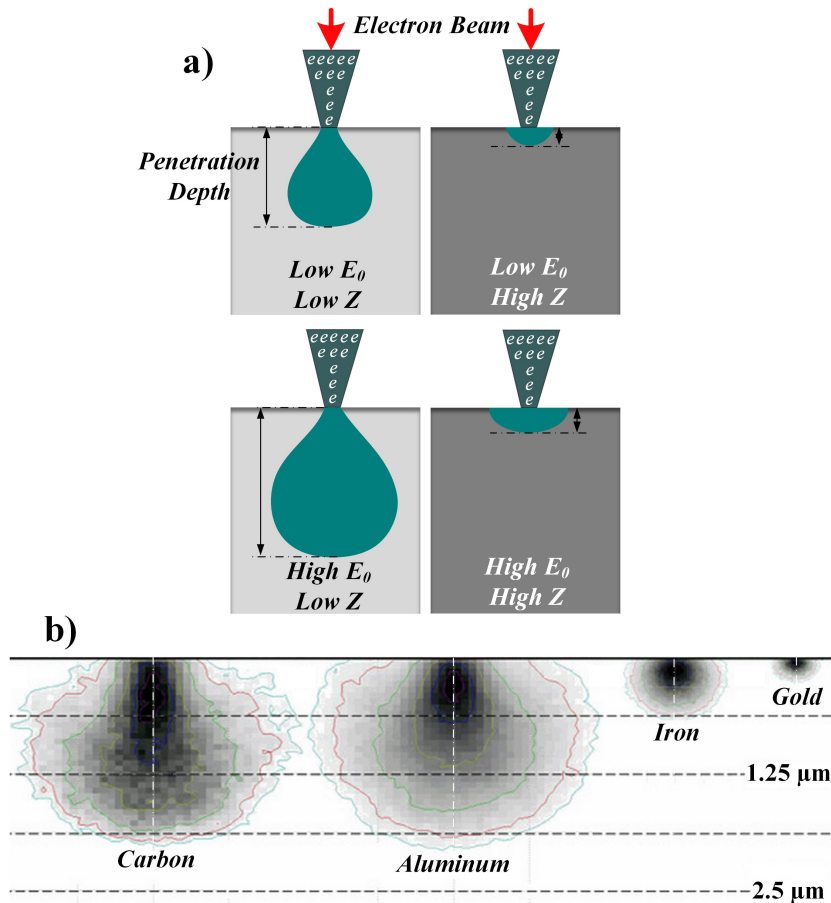
Fig. 15. *(a) An illustration showing the interaction volume profiles for low and high Z and E_0 values, (b) Monte Carlo simulations showing the shape of depth of the excitation volume in C, Al, Fe and Au (E0 for this experiment was 15 kV). Reproduced from [87], [89].*

5.4. Transmission Electron Microscopy (TEM)

Transmission Electron Microscopy (TEM) provides a unique opportunity to acquire high-resolution micrographs and achieve valuable information regarding the sample chemistry and crystallography [90]. Nevertheless, the method is costly and can be quite time consuming as compared to SEM. Similarly to the SEM, electron beam/sample interaction is what makes TEM analysis possible. Unlike the SEM, where micrographs are acquired by detecting SEs and BSEs that are emitted from the surface of a bulk sample, the TEM micrographs are recorded by detecting electrons that are *transmitted* through a thin foil sample, see **Fig. 16**. The foil thickness is typically in the range 20-200 nm depending on many factors such as the type of analysis, grain size, energy of the incoming electrons, etc. Transmitted electrons are either elastically scattered, inelastically scattered or unscattered. A definition and utilization of each type of transmitted electrons are as follows [82], [90];

- *Unscattered electrons* are incident electrons that are transmitted through the thin foil without any interaction taking place inside the sample. These electrons are inversely proportional to the sample thickness. Accordingly, thicker regions of the sample will have less number of transmitted unscattered electrons and hence will appear darker, conversely the thinner regions result in a higher number of transmitted unscattered electrons and hence will appear lighter in a TEM image, see below.

- *Elastically scattered electrons* are incident electrons that are deflected from their original path by atoms in the thin foil in an *elastic* manner, *i.e.* they experienced (almost) no energy loss. These electrons follow Bragg's Law, and are therefore scattered according to $\lambda = 2d_{hkl}sin\theta$ (where d is the interplanar distance, θ is the diffraction angle and λ is the wavelength of the incident electron wave. They provide information concerning the orientation, atomic arrangements and phases in the region of interest.

- *Inelastically scattered electrons* are electrons that interact with the thin foil atoms in an *inelastic* manner, *i.e.* they lose energy through the interaction(s). They also contain useful information and can be employed for Electron Energy Loss Spectroscopy (EELS), Energy Filtered Transmission Electron Microscopy (EFTEM) analyses as well as for the formation of Kikuchi bands.
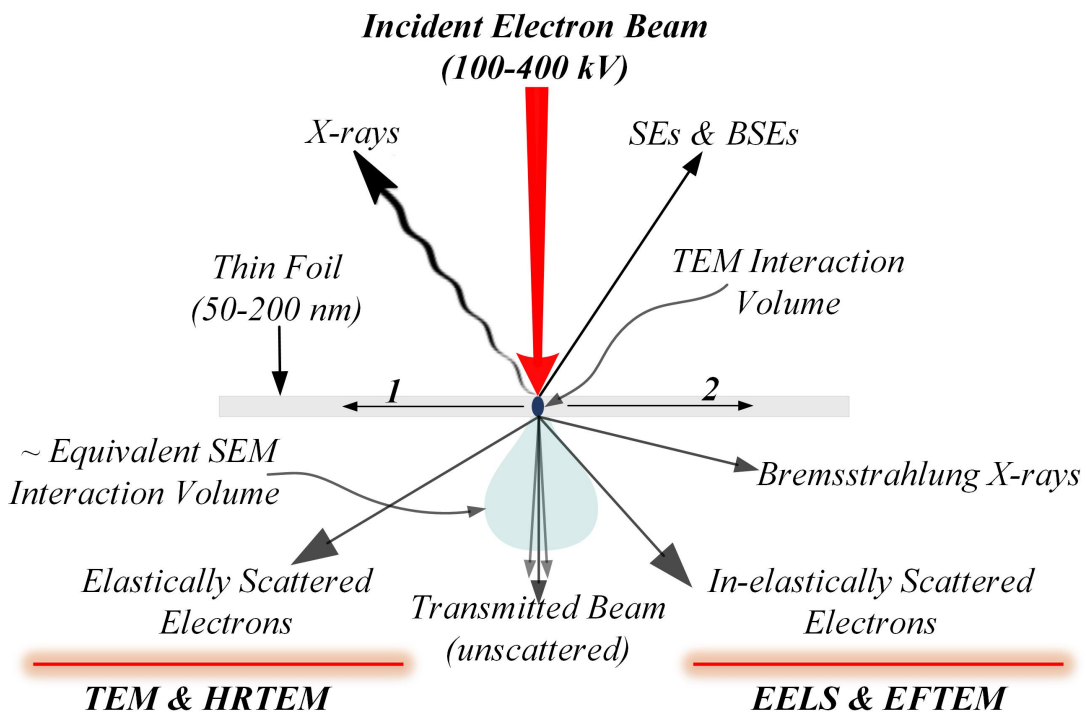
Fig. 16. *Schematic of electron-matter (thin foil) interactions arising from the impact of an electron beam onto a sample. Note: The arrows designated by 1 and 2 show "absorbed electrons" and "electron hole pairs". Reproduced from* [90].

TEM imaging can be performed in Bright Field (BF) and Dark Field (DF) modes. When the directly transmitted beam of electrons is selected, the resultant micrograph is a BF image, while a DF image is formed by detection of diffracted electrons. The approach of selecting electrons is to insert an aperture into the back focal plane of the objective lens [90]. In the case of the BF mode of the TEM, mass-thickness and diffraction contrast largely contribute to image formation, *i.e.* the regions containing high-Z atoms and grains with certain orientations fulfilling Bragg's law appear with dark contrast. In the case of the DF mode, an objective aperture is employed to select electrons that have been scattered by the thin foil. DF imaging provides valuable information concerning grain orientations, planar defects, stacking faults or particle size [82].

Scanning Transmission Electron Microscopy (STEM) imaging is different from TEM imaging. In this case, instead of parallel imaging, serial imaging is done by scanning a focused electron beam. In STEM mode, detectors are used instead of apertures but based on the same principle. Only electrons that are intended to contribute to the image formation are allowed to hit the detector. Thus, for STEM-ADF images an Annular Dark-Field (ADF) detector is centered on the optic axis. There is a hole in the middle of the detector within which the BF detector is located. The BF detector only picks up the forward-scattered or the unscattered electrons through small angles < approx. 3°, the angle depends also on the so called camera length. The ADF images are complementary to the BF images. There can be another detector called High-Angle ADF (HAADF) detector, which is located around the ADF detector and collects higher angle scattered electrons and offers Z-contrast images with minimum diffraction contrast, see **Fig. 17** [82], [90].

In this project, STEM analyses were widely employed to shed light on detailed microstructural information from the oxide layers as well as oxide/alloy interfaces (see papers I-IV). An FEI Titan 80-300 TEM/STEM equipped with a FEG operated at an accelerating voltage of 300 kV was used. The instrument is equipped with an Oxford Inca EDX detector. STEM images were captured in the BF and HAADF modes. Moreover, STEM/EDX was used to analyze the chemical composition of the microstructural features and corrosion products formed on the alloys. The electron

transparent cross-section specimens were produced by a site-specific thin foil preparation technique using a FIB/SEM, see below.
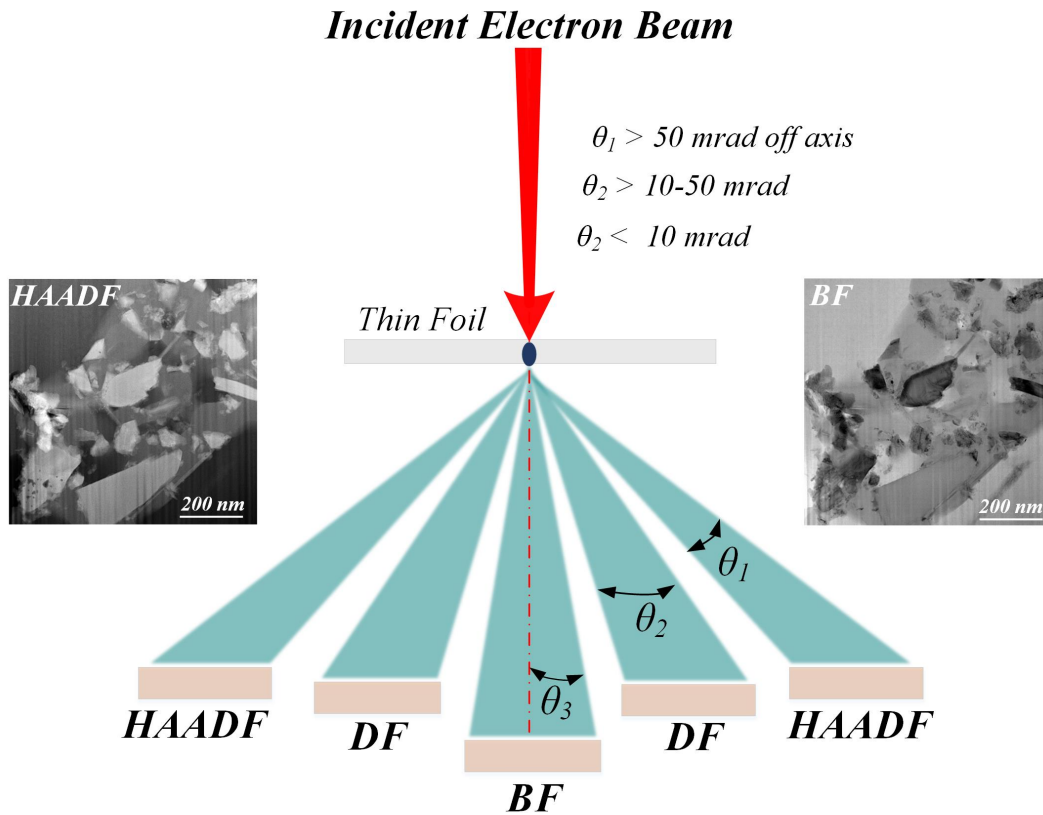
Fig. 17. *Schematic illustration showing the position of detectors for the BF, DF and HAADF imaging* [90]. *The HAADF and BF images in the figure show the microstructure of a Magnesium alloy reinforced by SiC particles.*

5.5. Transmission Kikuchi Diffraction (TKD) technique

The Transmission Kikuchi Diffraction (TKD) technique is a novel and innovative variant of the conventional Electron Backscattered Diffraction (EBSD) method and is used in the SEM. It was initially introduced by Keller *et al.* [91] at National Institute of Standards and Technology (NIST), USA, in 2012. Although the method is also known as transmission-Electron Backscatter Diffraction (t-EBSD) [91]–[93], the transmitted nature of the diffraction pattern projection (see **Fig. 18**) makes the term "backscatter diffraction" incorrect and thus more suitable name, TKD, has been used through this thesis. It should also be mentioned that the method is also referred to as transmission-Electron Forward Scatter Diffraction (t-EFSD) in some studies, see for example [94], [95].

Conventional EBSD provides a spatial resolution of, at best, 20 nm [96]. The TKD, which is also a SEM-based method, offers an improvement in spatial resolution over conventional EBSD [92], [93]. TKD analysis is carried out on thin foils (with thickness < 150 nm) instead of bulk samples (see **Fig. 18**). Hence, beam broadening is considerably decreased, and accordingly the spatial resolution is reduced to 2-5 nm in the best cases [97], [98]. Such spatial resolution is comparable to nano-diffraction techniques in TEM, such as Convergent Beam Electron Diffraction (CBED) [99]–[101]. However, the TKD is inexpensive (SEM-based), automated and fast as compared to other high-resolution nano-diffraction methods.
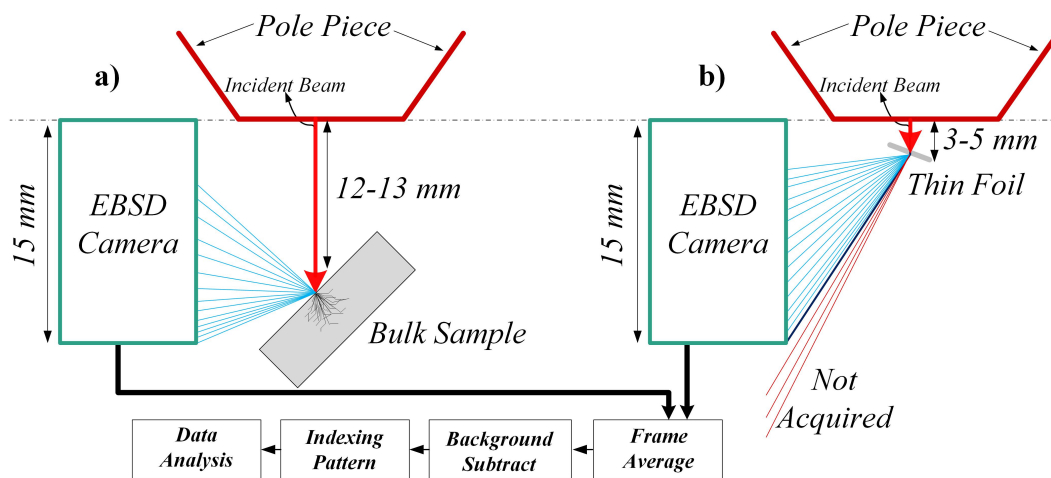
Fig. 18. *Schematic illustration showing the basic principles of electron detection and experimental set-up in (a) conventional EBSD and (b) TKD.*

Here it is appropriate to briefly discuss the difference between conventional EBSD and TKD in terms of the scattered electrons being detected by the phosphorous screen in each method (see **Fig. 18**). In conventional EBSD, when primary electrons hit a bulky specimen, they may be scattered by means of elastic and inelastic scattering events (see **Figs. 16** and **18**) and produce diffusely scattered electrons emitted in many different directions. At the final stage (as the last event), one Bragg scattering event must occur in order to obtain crystallographic information from the specimen. In order for many of the scattered electrons to be detected, the bulk sample is tilted 70º towards the detector on the side. However, tilting reduces the spatial resolution by a factor of three since the excitation volume becomes oval. During each scattering event energy is lost and since the excitation volume is relatively large, the total energy lost is high and different for every electron according to the number of events. More scattering events mean more energy lost, which means more difference in wavelength

of the scattered electrons. As a result, different electron energies and consequently different electron wave lengths lead to blurry EBSD patterns and thus reduces the signal/background ratio of the ordinary EBSD [91].

In TKD, however, it is forward scattered or transmitted electrons (TEs) that form Kikuchi bands as compared with conventional EBSD technique where backscattered electrons form the bands. Thus, the energy of the scattered electrons is more or less the same, which results in high-quality patterns. Besides, in TKD, there is little beam-spreading as the interaction volume is smaller in thin specimens [91].

In this project, the TKD analyses were carried out using an HKL Channel 5 EBSD system with a Nordlys II detector, mounted on a Zeiss Ultra FEG SEM. The TKD data were collected from thin foils, which were cross-sectioned through the oxide scale and the metal substrate. The experiments were performed using a new TKD sample holder designed at Chalmers University of Technology within this project, more details regarding the optimum microscopic parameters and the sample holder is provided in the next chapter.

5.6. Focused Ion Beam Milling (FIB)

Over the past decades, Focused Ion Beam (FIB) microscopy has been extensively used in fundamental materials studies and technological applications, since it offers high-resolution imaging and flexible micro-machining, simultaneously [102]. Such micro-machining allows fabricating site-specific cross-section through, for instance, oxide scales on metal substrates with a minimum amount of artifacts as compared to mechanically prepared cross sections. The FIB is also recognized as a technique for fabricating high-quality and thin (< 100nm) TEM foils [102].

A versatile "dual-beam" platform (FIB/SEM workstation) comprises a gallium focused ion beam (FIB column) in addition to an electron beam (SEM column), see **Fig. 19**. It is therefore possible to conduct SEM imaging, deposition (usually at length scales of a few tens of nanometers to hundreds of microns) as well as milling procedures in the same instrument [102].

In the FIB, interactions between ions and the sample are usually explained by the "collision cascade" model (**Fig. 19c**). This model involves a series of independent binary collisions. Thus, if the translational energy transferred to a target atom during a collision exceeds a critical value, the atom will be knocked out of its original site, for example, generating an interstitial-vacancy pair in a crystalline specimen, for more details see [102].
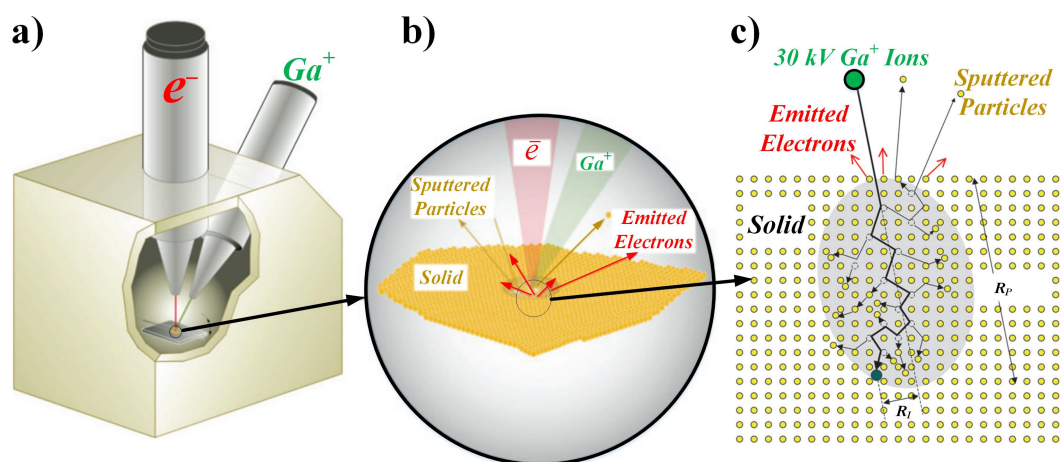
Fig. 19. *Schematic illustration showing (a) a dual-beam FIB/SEM instrument, (b) the electron and ion beam specimen interaction, (c) an illustration showing a collision cascade generated by Ga^+ ions incident on a crystal lattice of a solid. It also illustrates the damage generated in the collision cascade volume. Note: In Fig. 6c, R_p stands for the projected range and R_l is the lateral range of the implanted ion. Reproduced from [102], [103].*

The FIB method was used in this project to fabricate single-sided cross-sections (papers I and II) and thin foils for TKD (papers III and IV) and STEM (all papers) analyses using an FEI Versa 3D combined FIB/SEM workstation. FIB-prepared cross-sections through the corrosion layers and the subjacent metal were made when a precise positioning of the cross-sections was required. Single-sided cross-sections were fabricated at 0º tilt, providing cross-sections with the angle of 52°. However, SEM/EDX analyses on the cross-sections were carried out on a pre-tilted sample holder (see the SEM part of the Experimental section) in order to do the EDX analysis on the relatively horizontal area (with 7° tilt).

The site-specific *in-situ* lift-out procedure was employed in the FIB/SEM to produce smooth and damage-free thin foils using the following procedure; Platinum (Pt) deposition, course ion milling (bulk-cut), U-cut, lift out, mounting on a copper grid, thinning and finally cleaning. Thus, after identifying the region of interest by the help

of the SEM column in the FIB/SEM instrument, a Pt-strip (20 μm× 4 μm) was first deposited *in-situ* with the aid of electrons for protecting the outermost layer of oxide scales for few minutes. Afterwards, a thicker Pt-layer (around 2 μm thick) was deposited with the aid of Ga ions for further protection of the oxide scales during the following milling procedure. Subsequently, coarse milling was performed on the two sides of the Pt-layer by Ga ions using an accelerating voltage of 30 kV and high ion currents. In order to create a smooth area around the Pt-strip, the ion current was successively decreased from 64 nA to 4.5 nA throughout the milling to produce a sample with a thickness of around 2 μm. The sample was then attached to an Omniprobe micromanipulator by the aid of Pt deposition and was then mounted on a copper grid. Final thinning was performed to fabricate an electron transparent thin foil sample using low ion current. In this way, thin foils with thicknesses less than 150 nm were produced.

5.7. In-situ ESEM investigations

Environmental Scanning Electron Microscopy (ESEM) was invented by a Greek-Australian physicist Gerasimos Danilatos while working at the University of New South Wales, Australia, in 1978 [104]. The instrument provides a unique opportunity to maintain a gaseous environment (like water vapor) around a specimen, while imaging throughout the experiment. Besides, ESEM analyses can be done in a variety of pressures (up to at least 10 Torr), temperatures (-30-1500ºC) and humidity [105]. The other advantage of using the ESEM is imaging of non-conductive specimens, wet or dry, without the necessity for conductive coatings [105]. These abilities offer a unique prospect to view dynamic processes occurring on the materials' surfaces *"live"*.

ESEM imaging employs the use of Gaseous Secondary Electron Detector (GSED) instead of an Everhart-Thornley (ET) detector, which is used in conventional SEMs. This detector works in vacuum, but at higher pressures than for standard SEM, see **Fig. 19**. By applying a positive potential to the GSED, the SEs emitted by the specimen are attracted towards the detector. As the electrons accelerate in the detector field, they collide with gas molecules which are present in the ESEM chamber. These ionizations generate additional electrons, thus amplifying original secondary electron signal. The detector collects the SE signal and passes it directly to an electron

amplifier. For nonconductive specimens the positive ions generated in the gas ionization process are attracted towards the specimen surface where they suppress charging artifacts. The ESEM can acquire electron micrographs from specimens as hot as 1500ºC (depending on the hot stage) as the GSED is insensitive to heat and to light.
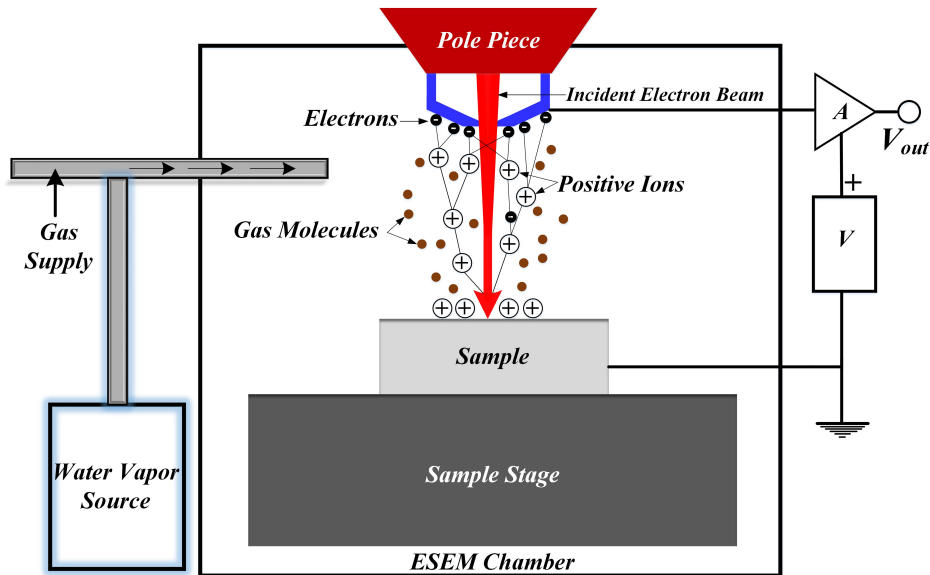
Fig. 19. *Schematic diagram showing the ESD that employs gas molecules to intensify the SE signals. In nonconductive specimens, positive ions are attached to the specimen surface as charge accumulates from the incident beam. Reproduced from* [105].

Since its invention, a wide range of fields including physics, chemistry, biology and medicine have successfully employed the ESEM technology. In addition, the understanding of the capability of ESEM has been improved across the diverse field of materials science, e.g. study of samples in dynamic processes, such as tension, compression, deformation, crack propagation, heating, cooling, freezing, melting, hydration, and dehydration [105], [106]. However, even if a number of studies investigated the use of ESEM in the abovementioned fields, the advantages of using the ESEM is not yet as mature and well-understood as conventional SEM, especially in the field of materials science due to the essential needs and considerations in preparation procedures and the difficulties associated with the pressure inside the microscope chamber [107].

Observing interactions between metal surfaces and environmental contaminations like gaseous species and alkali salts at the very early stages of oxidation, in the order of

minutes or hours, of metallic materials is one of the practical applications of ESEM *in-situ* experiments. Currently, ESEM technology has been established as a promising analytical technique for high-temperature corrosion experiments of stainless steels and ceramics [45-50]. Proff *et al.* [108] and Abolhassani *et al.* [109] reported the advantages of using of ESEM *in-situ* experiments in analyzing the oxidation behavior of Zirconium (Zr binary alloys and Zircoaloy-4) oxidized at temperatures more than 400ºC. In an early work done by Gerristead *et al.* [53], the ESEM was used to monitor dynamic corrosion processes taking place on a 316L stainless steel and the relevant corrosion mechanisms and the features that were most susceptible to corrosion were studied. In a number of published studies, Jonsson *et al.* [110], [111] have demonstrated the abilities of ESEM for investigating the oxidation behavior of several alloys including a Fe-2.25Cr-1Mo as well as pure iron in O_2 and $O_2 + H_2O$ environments in the temperature range of 400-600ºC.

In this thesis (papers I and II), an FEI Quanta 200 FEG ESEM (in ESEM-mode) was used to investigate the early stages of oxidation of two stainless steels, Sanicro 25 and Kanthal APMT as well as one Ni-base model alloy, TH1, in lab air at 450ºC and 4.8 Torr. The test coupons were cut by a low-speed saw to reach to the dimensions of $3 \times 3 \times 2$ mm^3 to be able to fit into the heating stage sample holder that was used for the ESEM *in-situ* exposures. Each coupon was ground using 600-4000 grit SiC sandpapers until the surface was mirror-like, followed by two polishing steps on cloth discs using diamond paste in the range 3-1 μm. Thereafter, the samples were cleaned carefully in acetone and ethanol using an ultrasonic bath. A a saturated solution of KCl in water/ethanol (20:80) was sprayed on the test coupons. The samples were dried with a cool air blower and stored in a desiccator awaiting the *in-situ* ESEM exposures.

ESEM imaging was done using the highest accessible accelerating voltage, *i.e.* 30 kV, to minimize the primary beam interaction with the gas inside the chamber. The temperature was ramped to the desired temperature using a ramp-up speed of 50°C/min. A new methodology was used to calibrate the sample temperature, which is discussed in detail in Paper (II). Post-exposure analyses, such as SEM imaging, SEM/EDX and TEM were performed on the *in-situ* ESEM and the corresponding reference tube furnace exposed specimens (see papers I and II).

6. Results and discussion

Four papers are included in this Licentiate thesis. Paper I and II present the very initial stages of oxidation of two alumina-forming alloys (TH1 and Kanthal APMT) and one chromia-forming alloy (Sanicro 25) by means of the *in-situ* ESEM oxidation technique in lab air, at 450ºC. In Paper III, the effect of isothermal and cyclic exposures on the oxidation behaviour of a Ni-base alloy HR-214 was studied up to 720 h at 1200°C. Paper IV reports on the feasibility of the TKD technique for analyzing fine-grained oxide scales formed on stainless steels and presents optimized analysis parameters as well as a newly developed thin foil holder.

This chapter consists of two main parts. The first presents the developments and optimizations of the TKD technique, in terms of thin foil holder, specimen preparation by FIB milling and acquisition parameters, while the second provides a summery of the appended papers.

6.1. Developments of the TKD technique

Up to the present time, many attempts have been carried out to improve the spatial resolution of EBSD, such as energy-filtered-EBSD and accurate deconvolution of EBSD patterns [112], [113] or using thin foils [114], [115]. Despite of such technological developments of the EBSD method, it still suffers from limited spatial resolution.

As mentioned in the Experimental part, the newly developed TKD technique is undoubtedly the most successful progress in improving the spatial resolution of the conventional EBSD, and thus it is now being widely employed in the diverse field of materials science. In this regard, Brodusch *et al.* [97] studied the generation process of the diffraction patterns using this technique and obtained crystallographic information from metallic nanoparticles with a size of ∼ 6 nm. In a number of recent publications, Trimby *et al.* [116]–[118] have demonstrated the potential of TKD grain boundary and orientation mapping for the automated analysis of nano-structured materials. Some other investigators have also reported the use of this method to characterize the microstructure of nano-structured metals [97], [119]. Babinsky *et al.* [92], [120] have effectively employed the TKD technique for analyzing Atom Probe Tomography (APT) specimens made up of pure molybdenum. Suzuki *et al.* [121] have obtained quantitative data from TKD maps of a thin film containing small-sized $Cr_{23}C_6$ carbides present in the microstructure of a Fe8Cr tempered martensitic steel sample. Bedekar *et al.* [122] have used the method to analyze the texture and orientation development in nanostructured hard turning layers of a low-alloyed steel. More recently, Wong *et al.* [123] have reported the use of TKD to study nano-sized grains in MgB_2 superconductors.

Despite of the attempts to employ the TKD for analyzing nano-structured metallic materials, much less effort has been devoted to study nano-sized grains in the oxide scales formed on metals in corrosive environments at high temperatures. Garner *et al.* [93] and Hu *et al.* [124], who are the only investigators to use the technique for analyzing nano-sized oxide scales, examined the microstructure and microtexture of zirconium oxide films formed on nuclear-grade zirconium alloy (Zircaloy-4). They referred to the TKD technique as an "ultra-high-spatial-resolution grain mapping" method, as it provided useful information on the crystal structure of grains as small as

5 nm. However, the authors in the later study [124] stated that they reached an indexing rate of only ~ 40% in their TKD maps. This basically means that 60% of the data were missing and therefore extracting some of the statistical data, such as grain size distribution and grain boundary character, was difficult and in some cases impossible. There is no study (except [125] and Paper IV in this thesis) on the use of the TKD method to analyze nano-grained oxide scales formed on any type of stainless steels at high temperatures.

In this project, a significant attempt has been performed to expand the application of the TKD grain boundary and orientation mapping (with indexing rates of > 85%, *i.e.* data-rich orientation maps) towards high-temperature corrosion studies of two alloys, namely Kanthal APMT and Haynes 214. To achieve such data-rich TKD orientation maps, it is imperative to understand the role of (*a*) *sample holder*, (*b*) *specimen preparation* and (*c*) *acquisition parameters* on obtaining high-quality TKD maps. These are briefly described below.

a) ***Designing the TKD experimental set-up*** Instabilities (in terms of both mechanical and beam drift) must be minimized to achieve high indexing rates in the TKD analysis. While the same hardware as for EBSD is used, the TKD setup is slightly different with regards to the sample position. Various sample holders have been employed for the TKD analysis. **Figure 20** shows two examples of the holder used by Birosca *et al.* [119] (**Fig. 20a**) and Meisnar *et al.* [126] (**Fig. 20b**). One common feature in these set-ups is the tilted SEM stage. It has, however, been reported that stage tilting can introduce mechanical instabilities.
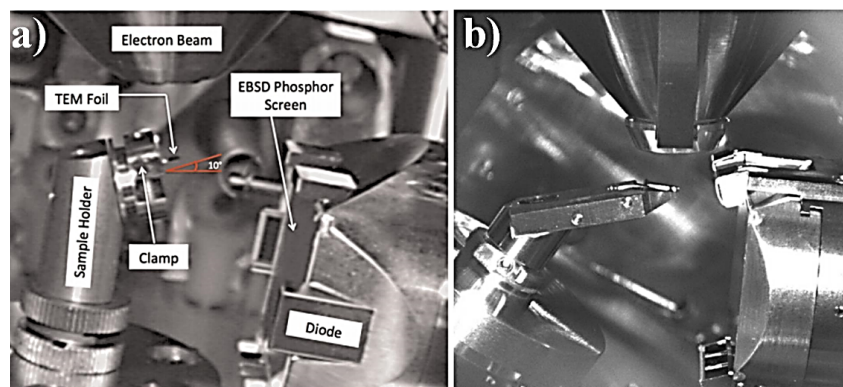
Fig. 20. *Two examples of TKD configurations used by (a) Birosca et al. [119] and (b) Meisnar et al. [126].*

As the TKD analysis is frequently conducted at high magnifications (100,000X), even small amounts of mechanical drift can considerably affect the indexing rate of the TKD analysis. Besides, most of the holders similar to the one used in **Fig. 20a** and in [98] limit the working distance (WD), *i.e.* the distance from the thin foil to the SEM pole piece, to large values (> 4 mm). Thus, in order to minimize such instabilities, a new thin foil holder was designed in this project, see **Fig. 21**. The brass holder in **Fig. 21a** was manufactured to position the copper lift-out grid, containing the thin foil, into the small thin foil holder that was later attached to the main sample holder, as shown in **Fig. 21b**. This new holder allows performing the TKD investigations at a small WD (~ 2 mm), *i.e.* a small gap between the thin foil and the pole piece of the microscope. The holder is designed in a way that the thin foil can be placed at 0°, 20° and -20° tilt allowing the detection of Kikuchi patterns from different angles. Furthermore, the holder gives the ability to insert a STEM detector below the sample and capture STEM images exactly at the location where the patterns were obtained and thus achieving imaging and crystallographic information, as well as chemical composition analysis by simultaneously using an EDX detector.
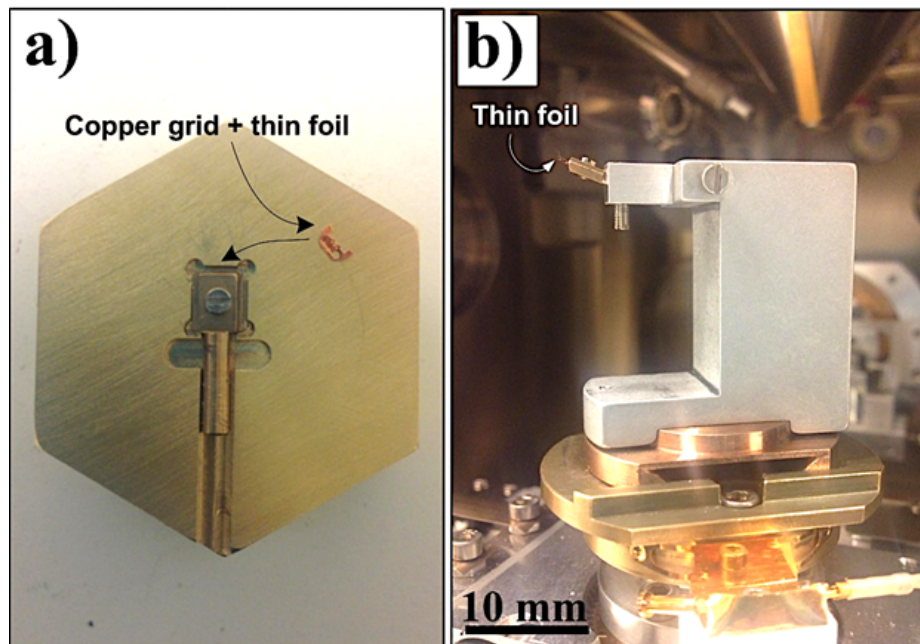
Fig. 21. (a) *The holder (made of brass) for positioning the copper grid, (b) An image of the new designed sample holder (made of aluminium) developed for the TKD experiments.*

b) *Sample preparation for the TKD analysis* Electrolytic polishing (electropolishing) and ion beam milling are dominating methods for preparing thin foils for TEM and TKD analyses. Although it is possible to produce defect-free samples by electropolishing, it may be somewhat more challenging for the cases of multiphase materials or specimens containing numerous intermetallic particles. Besides, it can be quite challenging to study the oxide/alloy substrate interfaces by this technique. FIB milling, on the other hand, delivers the benefits of site specificity; nevertheless, FIB milling can result in the introduction of artifacts, such as point defects and implantation of heavy gallium ions, near both surfaces of the specimen [127], [128]. An attempt was done in this project to optimize the milling procedure of the thin foils for the TKD analysis. It was found that high-quality polished surfaces of the thin foils are of great importance for achieving TKD maps with high indexing rate. Hence, lower accelerating voltages, i.e. 5 kV and 2 kV with ion currents of 48 pA and 27 pA respectively, were used in the final thinning processes. It should be emphasized that it is impossible to achieve high indexing rates from thin foils that are not appropriately prepared for the TKD analysis.

c) *Optimizing the acquisition parameters* High-quality TKD maps are only attainable when the right sets of acquisition parameters are used. Identification of the optimized parameters was carried out in this project. An accelerating voltage of 30 kV in high current mode and an aperture size of 120 μm were used to maximize the signal (Zeiss Ultra SEM). The highest voltage and current were used to maximize signal and they were kept constant throughout the experiments, as changes only would lead to poorer result for the thin foil samples. Even with the highest possible current and aperture size the probe size was still small enough, i.e. smaller than the spatial resolution of the TKD technique. Dynamic stretch was switched off and brightness and contrast level of the Kikuchi bands were manually set in a manner to obtain as high value of mean angular deviation (MAD) as possible and accordingly to achieve sufficiently high indexing rates. The mapping was performed at a working distance (WD) of 3.5 mm, with a step size ranging from 5 to 10 nm, a tilting angle of 20° and a dwell time of about 0.18 seconds per pattern (s/pt).

Using the right TKD configuration, the right FIB milling procedure and the right sets of acquisition parameters, the potential of the TKD method for investigating micro-grained and nano-grained oxide layers was evaluated. Besides, WD and specimen thickness were optimized. Below, the results related to the optimization of WD and the thin foil thickness of alumina samples are presented.

6.1.1. Optimizing the thin foil thickness

Micro-grained alumina These samples were essentially used as references, as they were composed of sufficiently large grain size, *i.e.* much larger than the thin foil thickness (~100 nm), in order to eliminate the effect of superimposed patterns (from overlapping grains), and thus making it possible to investigate the pure effect of sample thickness. **Figure 22** presents the percentages of the indexable patterns for the thin foils with different thicknesses as bar charts and also provides the quantitative data regarding the effect of foil thickness on the Pattern Quality (PQ). The PQ and indexing data followed the same trend in the case of micro-grained alumina. The highest PQ and indexing level were obtained from the sample with the thickness range 100-150 nm and then decreased with increasing thin foil thickness for the case of micro-grained alumina. It should be noted that the thinnest sample (thickness range 50-100 nm) showed poorer PQ and lower indexing level than the sample with thickness range 100-150 nm.

Nano-sized alumina scale The PQ values and percentages of the indexable patterns for the thin foils of the nano-sized alumina oxide scale are also provided in **Fig. 22**. As a general trend, PQ and indexing level decreased with increasing foil thicknesses. Interestingly, the highest indexing values were achieved not from the foil with the thickness range 100-150 nm (the optimum foil thickness for the case of micro-grained alumina), but from the thinnest foils with the thickness range 50-100 nm.

It is noticed that the PQ for the thinnest foil, 50-100 nm thick, was about twice than that of the thickest studied thin foil, i.e. 350-400 nm. The difference in indexing level was even more significant, being almost 10 times higher for the thinnest thin foils than that of the thickest ones. In fact, TKD mapping was

meaningless, or virtually impossible, when the thickness of the thin foils was more than 300 nm.
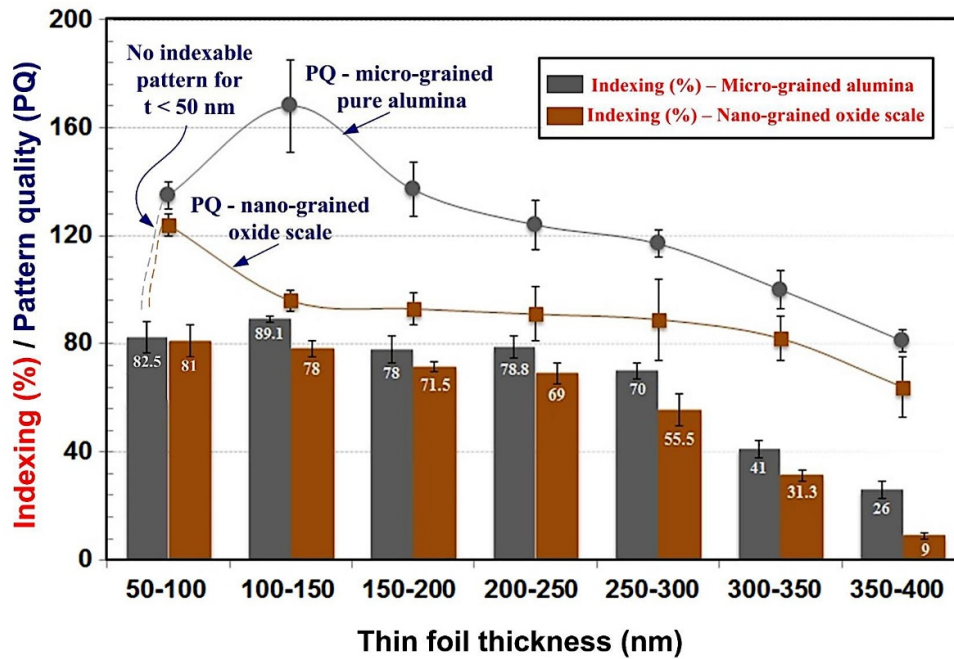

Fig. 22. The pattern quality data and indexing vs. the thickness of the foils for the micro-grained alumina and the nano-grained oxide scale developed on the alloy APMT.

One key finding was that the PQ values, as well as the indexing levels, dropped suddenly and the patterns exhibited a featureless background when the thin foil thicknesses were somewhere below 50 nm. In fact, it was not possible to collect indexable patterns from the thin foils with the thicknesses less than 50 nm. This can be attributed to the insufficient volume in terms of the occurrence of both the inelastic and elastic scattering events required for the TKD method.

6.1.2.   *Optimizing the WD*

The effect of WD on PQ was also studied on nano-grained alumina samples with an optimum thickness (50-100 nm), see **Fig. 23**. As mentioned earlier, the new sample holder enabled to examine the effect of WD even at short WDs (less than 3 mm). A separate EBSD calibration file and background acquisition was used for each WD. The results showed that PQ did not change considerably (around 140) when the WD was between 2 and 4 mm. However, it decreased markedly as WD increased from 4 to 8 mm. The corresponding value for the largest WD distance (8 mm) was 75, which corresponds to blurry diffraction patterns.

49
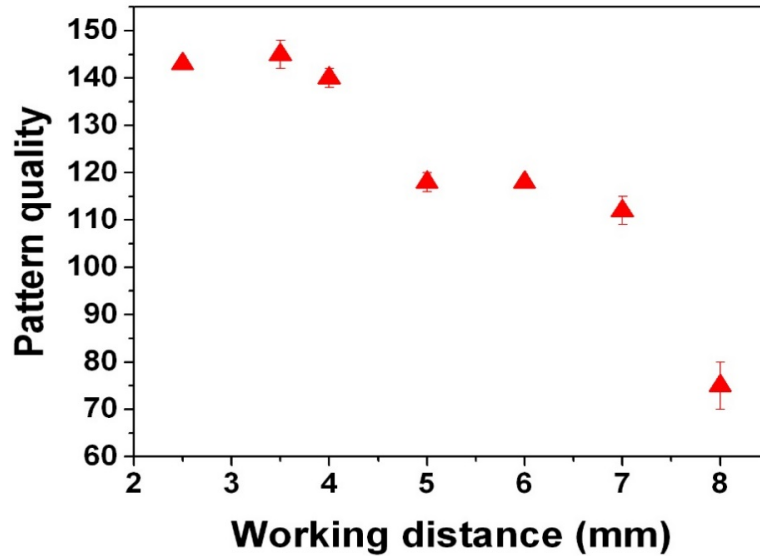
Fig. 23. *The TKD PQ data versus working distance for the thin foils of nano-sized alumina scale (sample thickness of 50-100 nm).*

Indeed, indexing of the TKD patterns was almost impossible for WDs larger than 7 mm using the geometrical set-up of our system. Although a relatively large range of WDs resulted in acceptable phase detection using the TKD patterns, the indexing rate decreased significantly (by a factor of 3) when the WD was increased from 4 to 6 mm. These results showed that WD has a great impact on the indexing level of the thin foils, reaching the maximum value of about 85 % when the WD was set to be ≤ 4 mm.

To understand the effect of WD on PQ it is necessary to calculate the minimum and maximum deflection angle (α) of the scattered electrons as a function of WD from the geometrical setup of the system, see **Fig. 24a**. The calculated α_{min} values of scattered electrons as a function of WD for our experimental set-up are presented in **Fig. 24b**. These angles were calculated based on the position of the EBSD detector and the vertical distance of the sample relative to the bottom part of the detector. Quite evidently, α_{min} increases with increasing the WD; *i.e.* when WD is shorter, scattered electrons with a smaller α_{min} can be collected by the EBSD phosphorous screen. For instance, when the analysis is carried out at the larger WD (8 mm) α_{min} was $\sim 32°$ meaning that the EBSD detector can only detect electrons having scattered angles larger than 32°. When WD was 2.5 mm, α_{min} was 25.5º, which means more scattered electrons could be detected by the EBSD phosphorous screen, and accordingly a higher PQ could be obtained, see **Fig. 23**.
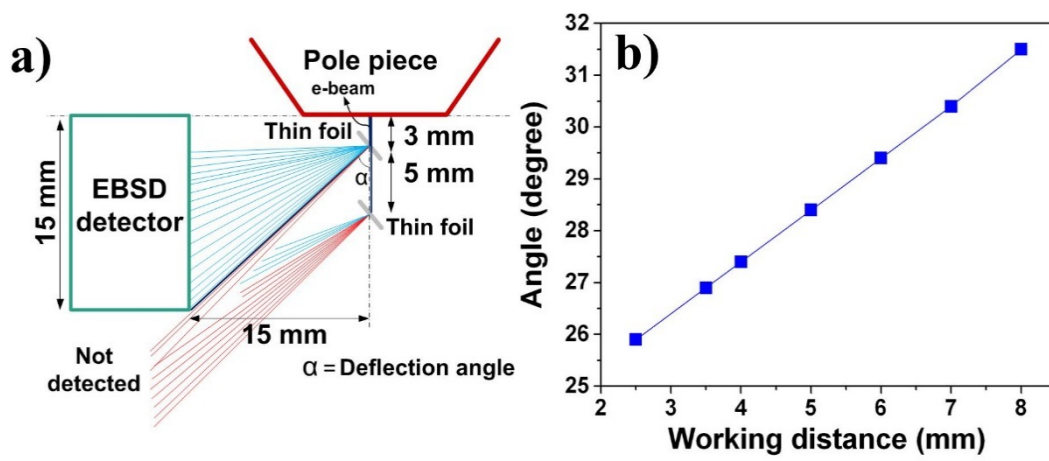
50

Fig. 24. *(a) A schematic illustration showing the position of the deflection angle (α) in the experimental set-up and (b) calculated α vales for different WDs.*

Paper I - *In-situ* ESEM investigation of KCl-induced corrosion of a FeCrAl and a model FeNiCrAl alloy in lab air at 450°C

The development of new high-temperature stainless steels has become technologically significant in many industries, especially in those that produce green electricity in boilers fired by biomass and municipal waste. Alumina-forming high temperature materials are one of the crucial material choices in such application. In this study, we examined the initial stages of oxidation of two alumina-forming alloys, FeNiCrAl (TH1, model alloy) and FeCrAl (Kanthal APMT) by means of *in-situ* ESEM exposures in lab air at 450°C. Similar to the previous study, ex-situ exposures were carried out by tube furnaces for reference. Both alloys were corroded in a matter of minutes. In addition to the local formation of oxide crusts and oxide shells (see **Fig. 25**), which were composed of Fe, Cr and Al oxides, a thin base oxide hosting numerous nodules was formed on the alloys' surfaces. Most notably, while alloy TH1 effectively resisted internal oxidation, alloy Kanthal APMT suffered alumina precipitates within the alloy. The underlying reason behind the superior oxidation behavior of the alloy TH1 was discussed by the aid of the so-called third-element effect (TEE) concept, i.e. higher ratio of Cr/Fe in the alloy and the formed scale. STEM/EDX analysis showed the presence of chloride, *i.e.* chlorination, at the scale/alloy interface for alloy TH1 and at the internal oxide precipitates in alloy Kanthal APMT.
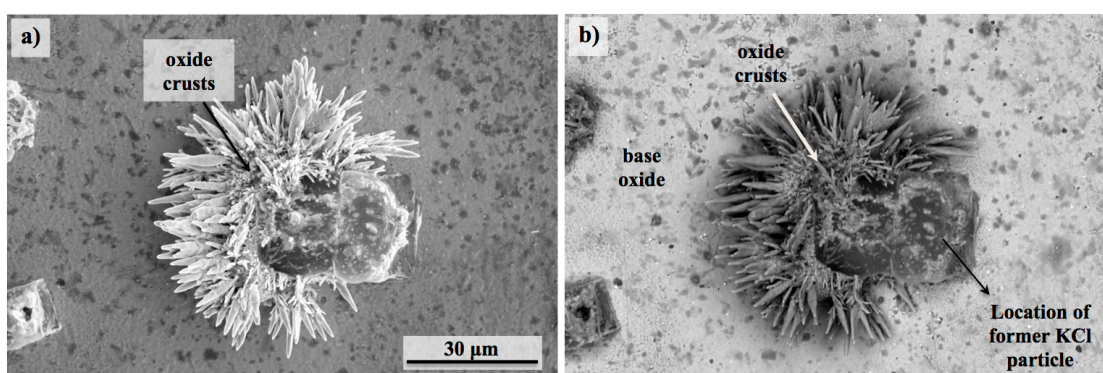
Fig. 25. *Plan view a) SEM-SE and b) SEM-BSE micrograph of alloy TH1 exposed in-situ ESEM for 1h at 450°C.*

Paper II - Investigating the initial stages of oxidation of a chromia-forming steel at 450ºC using environmental scanning electron microscopy

Initial stages of oxidation have an impact on the overall oxidation behaviour of high-temperature materials. This paper reports on the very early stages (up to 1 h) of a chromia-forming FeNiCr alloy Sanicro 25 by means of the *in-situ* ESEM technique in an O_2/H_2O gaseous environment at 450ºC. In this work, we showed that a precise temperature calibration of the ESEM hot stage is required for performing a reliable oxidation experiment using *in-situ* microscopy. The results of the *in-situ* ESEM exposure were validated by reference tube furnace exposures. Surface morphology and chemistry of the oxide scale and oxide crusts grown on the alloy surface were studied using SEM/EDX and STEM/EDX. It was shown that the presence of KCl particles in the studied environment is locally very corrosive even towards alloys Sanicro 25 as large oxide crusts (in the size range of several microns) were formed in the vicinity of KCl particles at this relatively low temperature and short exposure time, see **Fig. 26**. Within the time frame of oxidation, a thin (in the range 40-100 nm) base oxide was present on the main part of the surface. STEM/EDX studies showed that this layer was a double layer, the top layer being rich in iron oxide, while the bottom layer was chromia-rich. An oxidation-affected zone (OAZ), enriched in elements like Cu and Ni and depleted in Cr, was developed beneath the Cr-rich corrosion products.
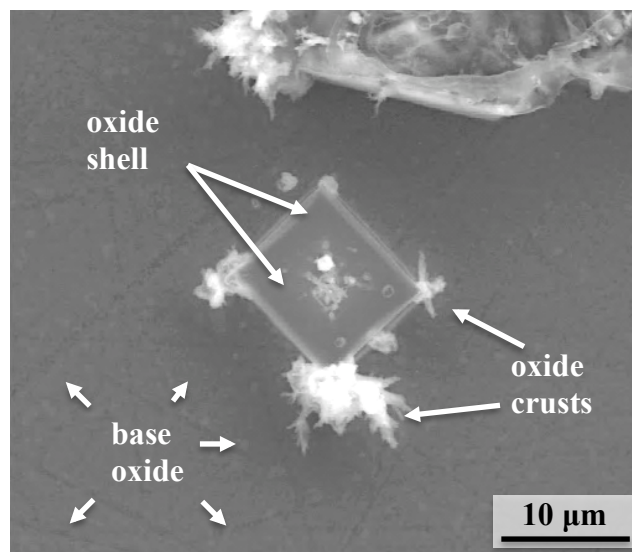
***Figure 26.** In-situ ESEM-SE micrographs captured after the exposure of Sanicro 25 in lab air for 1h at 450°C.*

Paper III - Effect of thermal cycling on protective properties of alumina scale grown on thin Haynes 214 foil

Alloy HAYNES 214 (HR-214) is one of the most suitable materials for thin-section heat exchangers. However, thin-walled components made of high-temperature materials may suffer from a critical Al depletion after a certain time, and consequently breakaway oxidation occurs. In this work, we clarified the effect of thermal cycling on the oxidation behavior of thin HR-214 foils (130 μm-thick) in air at 1200 °C for a time interval of 100-720 h. The microstructure of the oxide scales was analyzed by SEM/EDX, STEM/EDX and the TKD technique. The alloy developed a double layered scale composed of alumina and a mixed $Ni(Al,Cr)_2O_4$ spinel with minor inclusions of $(Cr,Al)_2O_3$ inside the spinel. When the Al content of the foil was finished a TACS (transition from external alumina to chromia scaling) happened at the oxide/alloy interface, i.e. the alloy turned from an alumina former into a chromia former during the oxidation. Besides, the results showed that Cr was transported by two mechanisms; (a) through the thermal cycling-induced vertical cracks in the oxide scales and (b) alumina grain boundaries (GBs), see **Fig. 27**. In this study, the TKD revealed that oxide grains were not textured but that a crystallographic orientation relationship close to $(111)_{spinel}$ // $(0001)_{corundum}$ was present at the spinel/alumina interface.
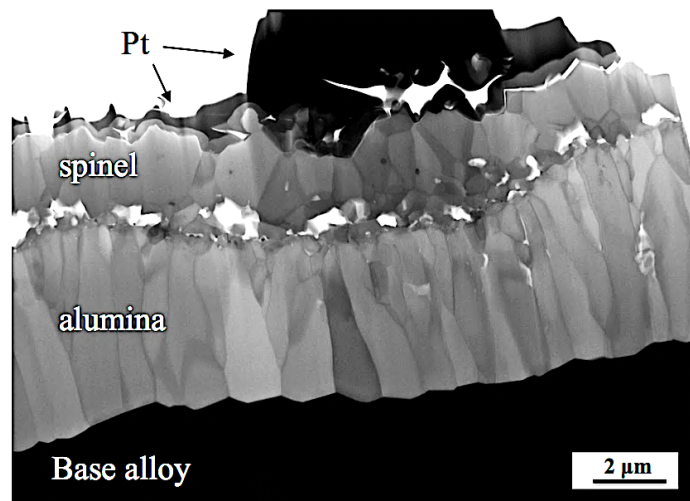
Fig. 27. STEM-BF micrograph showing the oxide scale morphology on HR-214 after 100 h isothermal exposure in air at 1200℃.

Paper IV - The capability of Transmission Kikuchi Diffraction technique for characterizing nano-grained oxide scales formed on a FeCrAl stainless steel

The goal of this paper is to report the potential of the TKD technique for analyzing the microstructure of the nano-sized oxide scales formed on stainless steels. The microstructure of oxide scales formed on an alumina-forming FeCrAl alloy, Kanthal APMT, in a dry and a wet environment for 24 and 168 h were analyzed. The newly developed thin foil holder and the optimized parameters in order to achieve high-quality TKD maps from nano-sized oxide scales were introduced. The TKD was also effectively employed for phase identification and texture analysis of the nano-grained oxide scale, containing grains as small as 20 nm, formed on a FeCrAl alloy. The results showed that an orientation relationship $(110)_{bcc}$ // $(0001)_{corundum}$ was present at the substrate/oxide scale interface. A notable finding of this study was the detection of *one* small grain (~ 40 nm) with a cubic (spinel-type) structure, which was located in the outer oxide scale layer (all other grains corundum) formed on the alloy exposed to the wet environment for 168 h at 1100 °C by the TKD technique. In order to validate the TKD result, the same region studied by the TKD was also studied by STEM/EDX (see **Fig. 28**).
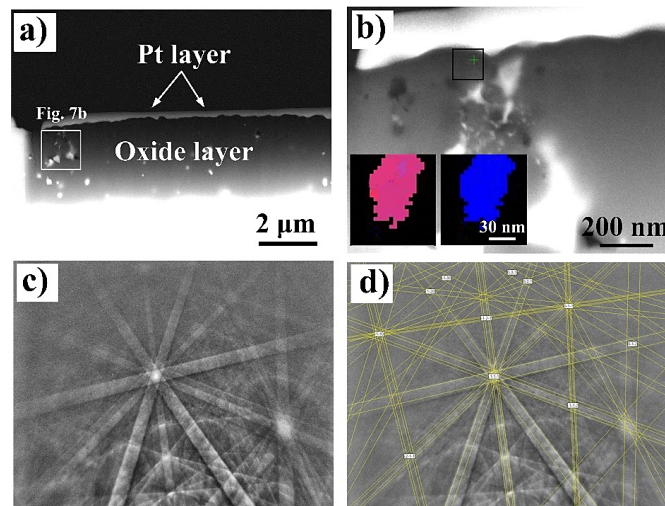
Fig. 28. *(a) An overview of the of a FIBed cross section on the alloy Kanthal APMT exposed to the wet environment for 168 h at 1100°C, (b) STEM-HAADF micrograph showing the investigated region by the TKD method and detection of a single nano-sized grain (~ 35 nm) in the designated rectangle with spinel structure in the outer oxide layer by TKD mapping (see the orientation map (red) and the phase map (blue) in the lower part of Fig. 7b), (c) and (d) the TKD patterns of the grain with spinel structure.*

Future work

The TKD technique was optimized, and thus it is possible to perform high-quality TKD maps on nano-sized oxide scales. In order further develop the technique and to acquire further acknowledge within research field the physics behind the technique will be evaluated in more details. In this regard, it is important to understand the contributions of elastic and inelastic scattering in generation of TKD patterns. Additionally, Monte-Carlo simulations can be used in order to predict optimized foil thickness and TKD parameters for other materials than alumina. Besides, more work is needed to effectively employ the technique in order to understand the crystallographic orientation relationship at interfaces, both at the oxide/oxide and at oxide/alloy interfaces (see an example in **Fig. 29**).
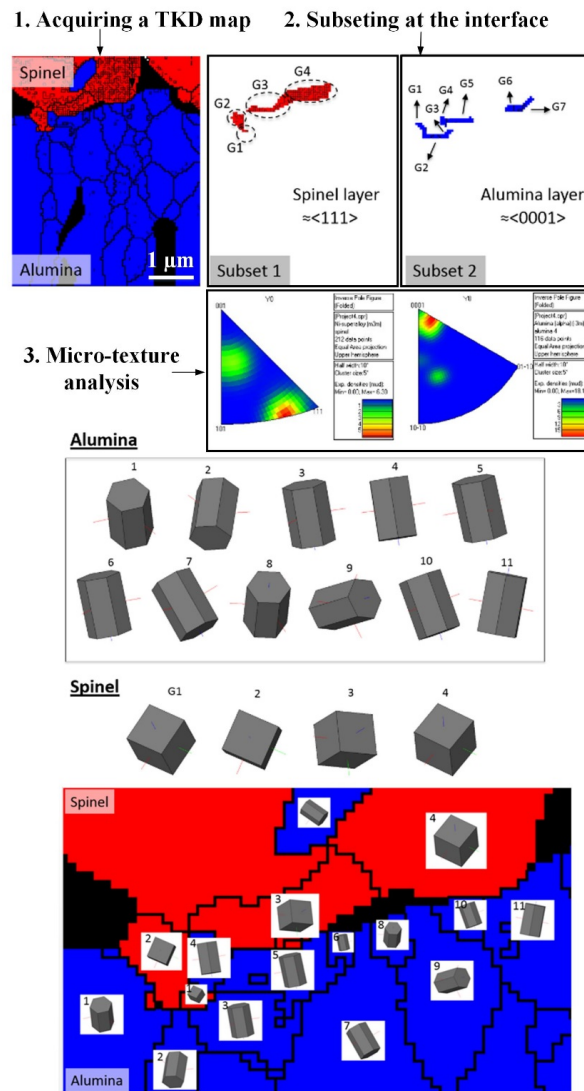
Fig. 29. *An example showing how it is possible to study the crystallographic orientation relationship at interfaces by the TKD technique.*

Figure 29 demonstrates an example analysis of such attempt showing an epitaxial relationship of close to $(111)_{spinel}$ // $(0001)_{corundum}$ at the alumina/spinel interface of alloy HR-214 exposed for 720 h in lab air at 1200°C. The TKD results showed that the planes of highest atomic density in alumina scale and spinel layer were very close to parallel.

Additionally, the aim of the project will be evaluating the protective character of the oxide scales that are formed on chromia and alumina formers in low pO_2 environments, *i.e.* N- and C-rich environments, at high temperatures. Corrosion mechanisms in low-pO_2 environments are not fully understood, especially for alumina forming alloys. Systematic exposures, both on alumina and chromia formers, are required to be carried out in such atmospheres. Post-exposure analyses using advanced analytical techniques including high resolution STEM (HR-STEM), FIB/SEM, BIB, STEM/EDX, EBSD and TKD will be conducted to shed light on the corrosion mechanisms of several high-temperature materials in low pO_2 atmospheres.

Bibliography

[1]   S. Evans. (2015, March 11). Five charts showing the EU's surprising progress on renewable energy [Online]. Available: http://www.carbonbrief.org

[2]   N. Birks, G. H. Meier, and F. S. Pettit, Introduction to the high-temperature oxidation of metals, 2nd ed. Cambridge, UK: Cambridge University Press, 2006.

[3]   J. Charles, J.-D. Mithieux, P.-O. Santacreu, and L. Peguet, "The ferritic stainless family: the appropriate answer to nickel volatility?," Rev. Métallurgie, vol. 106, no. 3, pp. 124–139, 2009.

[4]   H. K. D. H. Bhadeshia, R. W.K. Honeycombe, Steels (Microstructure and Properties), 3rd ed. Amsterdam, Netherland: Elsevier, 2006.

[5]   P. Kofstad, High Temperature Corrosion, London/New York: Elsevier Applied Science, 1988.

[6]   J. K. L. Lai, C. H. Shek, and K. H Lo, Stainless Steels: An Introduction and Their Recent Developments, SAIF Zone, Sharjah, UAE: Bentham Science Publishers, 2012..

[7]   D. J. Young, High Temperature Oxidation and Corrosion of Metals. The Netherlands: Elsevier, 2008.

[8]   R. Prescott and M. J. Graham, "The formation of aluminum oxide scales on high-temperature alloys," Oxid. Met., vol. 38, no. 3–4, pp. 233–254, 1992.

[9]   M. P. Brady, Y. Yamamoto, M. L. Santella, and L. R. Walker, "Composition, microstructure, and water vapor effects on internal/external oxidation of alumina-forming austenitic stainless steels," Oxid. Met., vol. 72, no. 5–6, pp. 311–333, 2009.

[10]   D. P. Whittle and J. Stringer, "Improvements in High Temperature Oxidation Resistance by Additions of Reactive Elements or Oxide Dispersions," Philos. Trans. R. Soc. A Math. Phys. Eng. Sci., vol. 295, no. 1413, pp. 309–329, 1980.

[11]   C. Houngninou, S. Chevalier, and J. P. Larpin, "High Temperature Oxidation Behaviour of Aluminide Coatings Obtained by Pack Cementation," in Materials Science Forum, 2004, vol. 461–464, pp. 273–280.

[12]   B. a Pint, A. Garratt reed, and L. W. Hobbs, "Analytical Electron-Microscopy Study of the Breakdown of α -Al2O3 Scales Formed on Oxide Dispersion-Strengthened Alloys," Oxid. Met., vol. 56, pp. 119–145, 2001.

[13]   P. Lours, J. Alexis, and G. Bernhart, "Oxidation resistance of ODS alloy PM2000 from 880 8 C to 1400 8 C," vol. 7, pp. 1089–1093, 1998.

[14]   P. Whittaker, "Powder Metallurgy Review,": Inovar Communications Ltd, Vol.3 No.4, Winter 2014.

[15]   Heat treatment furnaces - Kanthal. [Online]. Available: http://kanthal.com/

[16]   M. Mcguire, "Stainless Steels for Design Engineers", 1st ed. Materials Park, Ohio: ASM International, 2008.

[17]   S. Lampman, Weld Integrity and Performance: A Source Book Adapted from ASM International Handbooks, Conference Proceedings, and Technical Books: ASM International, 1997.

[18] J. M. Vitek, S. A. David, "The Sigma Phase Transformation in Austenitic Stainless Steels," Weld. J. Vol.65, pp 106-111, 1986.

[19] F. O. F. Supply, M. Properties, and M. Units, "Sanicro 25", vol. 05, 2015.

[20] T. Ishitsuka, Y. Inoue, and H. Ogawa, "Effect of silicon on the steam oxidation resistance of a 9% Cr heat-resistant steel," Oxid. Met., vol. 61, no. 1–2, pp. 125–142, 2004.

[21] Y. Nishiyama, Y. Sawaragi, T. Matsuda, S. Kihara, and I. Kajigaya, "Si content.pdf," Tech. reports, vol. No. 60 Dec, no. The sumltomo search, 1998.

[22] F. Masuyama, "History of Power Plants and Progress in Heat Resistant Steels," vol. 41, no. 6, pp. 612–625, 2001.

[23] F. O. F. Supply and M. Properties, "Sanicro 25 Tube and Pipe, Seamless Datasheet," 2008.

[24] R. Sandström, M. Farooq, and J. Zurek, "Basic creep models for 25Cr20NiNbN austenitic stainless steels," Mater. Res. Innov., vol. 17, no. 5, pp. 355–359, 2013.

[25] J. Zurek, S.-M. Yang, D.-Y. Lin, T. Hüttel, L. Singheiser, and W. J. Quadakkers, "Microstructural stability and oxidation behavior of Sanicro 25 during long-term steam exposure in the temperature range 600-750 °C," Mater. Corros., vol. 66, no. 4, pp. 315–327, 2015.

[26] Y. Yamamoto, M. L. Santella, M. P. Brady, H. Bei, and P. J. Maziasz, "Effect of alloying additions on phase equilibria and creep resistance of alumina-forming austenitic stainless steels," Metall. Mater. Trans. A, vol. 40, no. 8, pp. 1868–1880, 2009.

[27] A. O. Austenitic, S. Steels, and Y. Yamamoto, "Creep-Resistant, Al_2O_3-Forming Austenitic Stainless Steels," Science, vol. 433, no. 2007, pp. 2–6, 2011.

[28] C. Gindorf, L. Singheiser, and K. Hilpert, "Chromium vaporisation from Fe, Cr base alloys used as interconnect in fuel cells," Steel Res., vol. 72, no. 11–12, pp. 528–533, 2009.

[29] J. Froitzheim, H. Ravash, E. Larsson, L. G. Johansson, and J. E. Svensson, "Investigation of Chromium Volatilization from FeCr Interconnects by a Denuder Technique," J. Electrochem. Soc., vol. 157, no. 9, p. B1295-B1301, 2010.

[30] W. J. Quadakkers, J. Piron-Abellan, V. Shemet, and L. Singheiser, "Metallic interconnectors for solid oxide fuel cells – a review," Mater. High Temp., vol. 20, no. 2, pp. 115–127, 2003.

[31] D. J. Young and B. A. Pint, "Chromium volatilization rates from Cr_2O_3 scales into flowing gases containing water vapor," Oxid. Met., vol. 66, no. 3–4, pp. 137–153, 2006.

[32] T. M. Pollock and S. Tin, "Nickel-Based Superalloys for Advanced Turbine Engines: Chemistry, Microstructure and Properties," J. Propuls. Power, vol. 22, no. 2, pp. 361–374, 2006.

[33] Nicrofer 6025 HT-alloy 602 CA [Online]. Available online at available online at www.vdm-metals.com

[34] Haynes 214 alloy [Online]. Available online at https://www.haynesintl.com

[35] Y. Yamamoto, M. P. Brady, M. L. Santella, H. Bei, P. J. Maziasz, and B. A. Pint, "Overview of strategies for high-temperature creep and oxidation resistance of alumina-forming austenitic stainless steels," Metall. Mater. Trans. A Phys. Metall. Mater. Sci., vol. 42, no. 4, pp. 922–931, 2011.

[36]   M. H. Lagrange, A. M. Huntz, and J. H. Davidson, "The influence of Y, Zr or Ti additions on the high temperature oxidation resistance of Fe-Ni-Cr-Al alloys of variable purity," Corros. Sci., vol. 24, no. 7, pp. 613–627, 1984.

[37]   H. M. Tawancy and N. Sridhar, "High-temperature oxidation behavior of a Ni-Cr-Al-Fe-Y alloy," Oxid. Met., vol. 37, no. 3–4, pp. 143–166, 1992.

[38]   D. Delaunay and A. M. Huntz, "Fe-Ni-Cr-A1 ALLOYS," vol. 24, no. 1, pp. 13–25, 1984.

[39]   M. P. Brady, K. A. Unocic, M. J. Lance, M. L. Santella, Y. Yamamoto, and L. R. Walker, "Increasing the upper temperature oxidation limit of alumina forming austenitic stainless steels in air with water vapor," Oxid. Met., vol. 75, no. 5–6, pp. 337–357, 2011.

[40]   M. P. Brady, Y. Yamamoto, M. L. Santella, and B. A. Pint, "Effects of minor alloy additions and oxidation temperature on protective alumina scale formation in creep-resistant austenitic stainless steels," Scr. Mater., vol. 57, no. 12, pp. 1117–1120, 2007.

[41]   M. P. H. B. Gerhardus H. Koch, "Cost of Corrosion Study Unveiled," Nace Int., 2002.

[42]   D. R. Gaskell, Introduction to the Thermodynamics of Materials, 5th Ed. New York: Taylor & Francis, 2003.

[43]   J. Froitzheim. "The formation of a protective oxide scale", Handout for Corrosion course, Chalmers University of Technology, Gothenburg, Sweden, 2014.

[44]   A. Atkinson and R. I. Taylor, "Ni along grain boundaries in nickel oxide," Philos. Mag. A, vol. 43, no. 4, pp. 979–998, 1981.

[45]   D. A. Jones, Principles and prevention of corrosion. Prentice Hall, 1996.

[46]   M. Schütze, "Mechanical properties of oxide scales," Oxid. Met., vol. 44, pp. 29–61, 1995.

[47]   C. Gleitzer, "Electrical Properties of Anhydrous Iron Oxides," Key Eng. Mater., vol. 125–126, pp. 355–0, 1997.

[48]   P. K. Footner, D. R. Holmes, and D. Mortimer, "Oxidation of Iron–Chromium Binary Alloys," Nature, vol. 216, no. 5110, pp. 54–56, 1967.

[49]   R. J. Hussey and M. J. Graham, "The influence of reactive-element coatings on the high-temperature oxidation of pure-Cr and high-Cr-content alloys," Oxid. Met., vol. 45, no. 3–4, pp. 349–374, 1996.

[50]   H. Asteman, J. Svensson, M. Norell, and L. Johansson, "Influence of Water Vapor and Flow Rate on the High-Temperature Oxidation of 304L ; Effect of Chromium Oxide Hydroxide Evaporation," Oxid. Met., vol. 54, no. 1–2, pp. 11–26, 2000.

[51]   H. Asteman, J. Svensson, and L. Johansson, "Indication of Chromium Oxide Hydroxide Evaporation During Oxidation of 304L at 873 K in the Presence of 10 % Water Vapor," Oxidatio, vol. 52, pp. 95–111, 1999.

[52]   H. Asteman, J.-E. Svensson, and L.-G. Johansson, "Effect of Water-Vapor-Induced Cr Vaporization on the Oxidation of Austenitic Stainless Steels at 700 and 900°C," J. Electrochem. Soc., vol. 151, no. 3, pp. B141-B149, 2004.

[53]   C. Pettersson, J. Pettersson, H. Asteman, J. E. Svensson, and L. G. Johansson, "KCl-induced high temperature corrosion of the austenitic Fe-Cr-Ni alloys 304L and Sanicro 28 at 600 °C," Corros. Sci., vol. 48, no. 6, pp. 1368–1378, 2006.

[54] C. Pettersson, L. G. Johansson, and J. E. Svensson, "The influence of small amounts of KCl(s) on the initial stages of the corrosion of alloy sanicro 28 at 600°C," Oxid. Met., vol. 70, no. 5–6, pp. 241–256, 2008.

[55] J. Pettersson, J. E. Svensson, and L. G. Johansson, "Alkali Induced Corrosion of 304-Type Austenitic Stainless Steel at 600°C; Comparison between KCl, K2CO3 and K2SO4," Mater. Sci. Forum, vol. 595–598, pp. 367–375, 2008.

[56] J. Pettersson, H. Asteman, J. E. Svensson, and L. G. Johansson, "KCl induced corrosion of a 304-type austenitic stainless steel at 600??C; the role of potassium," Oxid. Met., vol. 64, no. 1–2, pp. 23–41, 2005.

[57] Y. Kim and T. Hsu, "A reflection electron microscopic (REM) study of α-Al$_2$O$_3$(0001) surfaces," Surf. Sci. Lett., vol. 258, no. 1–3, p. A596, 1991.

[58] J. Quadakkers and L. Singheiser, "Practical Aspects of the Reactive Element Effect," Mater. Sci. Forum, vol. 369–372, pp. 77–92, 2001.

[59] P. Y. Hou, "The Reactive Element Effect – Past, Present and Future," Mater. Sci. Forum, vol. 696, pp. 39–44, 2011.

[60] S. Chevalier, "What did we learn on the reactive element effect in chromia scale since Pfeil 's patent?," Mater. Corros., vol. 65, no. 2, pp. 109–115, 2014.

[61] I. Kvernes, M. Oliveira, and P. Kofstad, "High Temperature Oxidation of Fe-13Cr-xAl alloys in Air / H$_2$O vapour mixtures," Corros. Sci., vol. 17, pp. 237–252,1977.

[62] G. Hultquist, B. Tveten, and T. Norby, "Hydrogen in chromium: influence on the high-temperature oxidation kinetics in O$_2$, oxide-growth mechanisms, and scale adherence," Oxid. Met., vol. 52, pp. 221–233, 1999.

[63] S. Jianian, Z. Longjiang, and L. Tiefan, "High-temperature oxidation of Fe-Cr alloys in wet oxygen," Oxid. Met., vol. 48, no. 3–4, pp. 347–356, 1997.

[64] D. Caplan and M. Cohen, "The Volatilization of Chromium Oxide," J. Electrochem. Soc., vol. 108, no. 5, p. 438, 1961.

[65] F. Liu, H. Josefsson, J. E. Svensson, L. G. Johansson, and M. Halvarsson, "TEM investigation of the oxide scales formed on a FeCrAlRE alloy (Kanthal AF) at 900°C in dry O$_2$ and O$_2$ with 40% H$_2$O," Mater. high Temp., vol. 22, no. 3–4, pp. 521–526, 2005.

[66] H. P. Nielsen, F. J. Frandsen, K. Dam-Johansen, and L. L. Baxter, "Implications of chlorine-associated corrosion on the operation of biomass-fired boilers," Prog. Energy Combust. Sci., vol. 26, no. 3, pp. 283–298, 2000.

[67] D. A. Tillman, D. Duong, and B. Miller, "Chlorine in solid fuels fired in pulverized fuel boilerss-sources, forms, reactions, and consequences: A literature review," Energy and Fuels, vol. 23, no. 7, pp. 3379–3391, 2009.

[68] F. H. Stott and C. Y. Shih, "High-temperature corrosion of iron-chromium alloys in oxidizing-chloridizing conditions," Oxid. Met., vol. 54, no. 5–6, pp. 425–443, 2000.

[69] H. Asteman and M. Spiegel, "Investigation of the HCl (g) attack on pre-oxidized pure Fe, Cr, Ni and commercial 304 steel at 400°C," Corros. Sci., vol. 49, no. 9. pp. 3626–3637, 2007.

[70] A. Zahs, M. Spiegel, and H. J. Grabke, "Chloridation and oxidation of iron, chromium, nickel and their alloys in chloridizing and oxidizing atmospheres at 400-700°C," Corros. Sci., vol. 42, no. 6. pp. 1093–1122, 2000.

[71] H. J. Grabke, E. Reese, and M. Spiegel, "The effects of chlorides, hydrogen chloride, and sulfur dioxide in the oxidation of steels below deposits," Corros. Sci., vol. 37, no. 7. pp. 1023–1043, 1995.

[72] J.-M. Abels and H.-H. Strehblow, "A surface analytical approach to the high temperature chlorination behaviour of inconel 600 at 700°C," Corros. Sci., vol. 39, no. 1. pp. 115–132, 1997.

[73] F. H. Stott and C. Y. Shih, "The influence of HCl on the oxidation of iron at elevated temperatures," Mater. Corros., vol. 51, pp. 277–286, 2000.

[74] R. A. Antunes and M. C. L. de Oliveira, "Corrosion in biomass combustion: A materials selection analysis and its interaction with corrosion mechanisms and mitigation strategies," Corros. Sci., vol. 76, pp. 6–26, 2013.

[75] Y. S. Li, Y. Niu, and M. Spiegel, "High temperature interaction of Al/Si-modified Fe-Cr alloys with KCl," Corros. Sci., vol. 49, no. 4, pp. 1799–1815, 2007.

[76] J. Pettersson, C. Pettersson, H. Asteman, J. E. Svensson, and L. G. Johansson, "A Pilot Plant Study of the Effect of Alkali Salts on Initial Stages of the High Temperature Corrosion of Alloy 304L," Mater. Sci. Forum, vol. 461–464, pp. 965–972, 2004.

[77] Y. S. Li, M. Sanchez-Pasten, and M. Spiegel, "High Temperature Interaction of Pure Cr with KCl," Mater. Sci. Forum, vol. 461–464, pp. 1047–1054, 2004.

[78] H. P. Nielsen, F. J. Frandsen, and K. Dam-Johansen, "Lab-scale investigations of high-temperature corrosion phenomena in straw-fired boilers," Energy and Fuels, vol. 13, no. 6, pp. 1114–1121, 1999.

[79] Y. Shinata, "Accelerated oxidation rate of chromium induced by sodium chloride," Oxid. Met., vol. 27, no. 5–6, pp. 315–332, 1987.

[80] M. Spiegel, "Salt melt induced corrosion of metallic materials in waste incineration plants," Mater. Corros., vol. 50, no. 7, pp. 373–393, 1999.

[81] D. J. Young, A. Chyrkin, J. He, D. Grüner, and W. J. Quadakkers, "Slow transition from protective to breakaway oxidation of haynes 214 foil at high temperature," Oxid. Met., vol. 79, no. 3–4, pp. 405–427, 2013.

[82] S. Amelinckx, D. van Dyck, J. van Landuyt, and G. Van Tendeloo, "Electron Microscopy: Principles and Fundamentals," VCH Verlagsgesellschaft mbH, 2007.

[83] W. Zhou and Z. L. Wang, "Scanning Microscopy for Nanotechnology," New York, Springer, 2006.

[84] N. Tanaka, "Scanning Transmission Electron Microscopy of Nanomaterials: Basics of Imaging and Analysis,". 2014.

[85] R. Shimizu and D. Ze-Jun, "Monte Carlo modelling of electron-solid interactions," Reports Prog. Phys., vol. 55, no. 4, pp. 487–531, 1999.

[86] D. C. Joy, "Beam interactions, contrast and resolution in the SEM," J. Microsc., vol. 136, no. 2, pp. 241–258, 1984.

[87] D. Drouin, A. R. Couture, D. Joly, X. Tastet, V. Aimez, and R. Gauvin, "CASINO V2.42: a fast and easy-to-use modeling tool for scanning electron microscopy and microanalysis users," Scanning, vol. 29, no. 3, pp. 92–101, 2005.

[88] J. I. Goldstein, H. Yakowitz, D. E. Newbury, E. Lifshin, J. W. Colby, and J. R. Coleman, "Practical Scanning Electron Microscopy: Electron and Ion Microprobe Analysis," Plenum Press, New York, 1975.

[89] P. G. Kotula, M. R. Keenan, and J. R. Michael, "Automated analysis of SEM X-ray spectral images: a powerful new microanalysis tool," Microsc. Microanal., vol. 9, no. 1, pp. 1–17, 2003.

[90] D. B. Williams and C. B. Carter, "The Transmission electron microscope," 2009.

[91] R. R. Keller and R. H. Geiss, "Transmission EBSD from 10 nm domains in a scanning electron microscope," J. Microsc., vol. 245, no. 3, pp. 245–251, 2012.

[92] K. Babinsky, R. De Kloe, H. Clemens, and S. Primig, "A novel approach for site-specific atom probe specimen preparation by focused ion beam and transmission electron backscatter diffraction," Ultramicroscopy, vol. 144, pp. 9–18, 2014.

[93] A. Garner, A. Gholinia, P. Frankel, M. Gass, I. MacLaren, and M. Preuss, "The microstructure and microtexture of zirconium oxide films stiudied by transmission electron backscatter diffraction and automated crystal orientation mapping with transmission electron microscopy," Acta Mater., vol. 80, pp. 159–171, 2014.

[94] N. Brodusch, H. Demers, M. Trudeau, and R. Gauvin, "Acquisition parameters optimization of a transmission electron forward scatter diffraction system in a cold-field emission scanning electron microscope for nanomaterials characterization," Scanning, vol. 35, no. 6, pp. 375–386, 2013.

[95] R. Geiss, R. Keller, S. Sitzman, and P. Rice, "New Method of Transmission Electron Diffraction to Characterize Nanomaterials in the SEM," Microsc. Microanal., vol. 17, no. S2, pp. 386–387, 2011.

[96] A. Schwartz, K. Mukul, and B. L. Adams, Eds., "Electron Backscatter Diffraction in Materials Science," Springer Science, Business Media, LLC, 2000.

[97] N. Brodusch, H. Demers, and R. Gauvin, "Nanometres-resolution Kikuchi patterns from materials science specimens with transmission electron forward scatter diffraction in the scanning electron microscope," J. Microsc., vol. 250, no. 1, pp. 1–14, 2013.

[98] P. W. Trimby, "Orientation mapping of nanostructured materials using transmission Kikuchi diffraction in the scanning electron microscope," Ultramicrosco., vol. 120, pp. 16–24, 2012.

[99] S. Zaefferer, "A critical review of orientation microscopy in SEM and TEM," Cryst. Res. Technol., vol. 46, no. 6, pp. 607–628, 2011.

[100] G. Wu and S. Zaefferer, "Advances in TEM orientation microscopy by combination of dark-field conical scanning and improved image matching," Ultramicroscopy, vol. 109, no. 11, pp. 1317–1325, 2009.

[101] H. H. Liu, S. Schmidt, H. F. Poulsen, A. Godfrey, Z. Q. Liu, J. A. Sharon, and X. Huang, "Three-dimensional orientation mapping in the transmission electron microscope.," Science, vol. 332, no. 6031, pp. 833–834, 2011.

[102] L. A. Giannuzzi and F. A. Stevie, "Introduction To Focused Ion", Springer, 2005.

[103] C. A. Volkert and A. M. Minor, "Focused Ion Beam Microscopy and Micromachining," MRS Bull., vol. 32, no. 05, pp. 389–399, 2007.

[104] G. D. Danilatos and V. N. E. Robinson, "Principles of scanning electron microscopy at high specimen chamber pressures," Scanning, vol. 2, no. 2, pp. 72–82, 1979.

[105] D. Stokes, "Principles and Practice of Variable Pressure: Environmetal Scanning Electron Microscopy (VP-ESEM)," John Wiley & Sons, Ltd, 2009.

[106] U. Klement, Y. Yao, S. N. Mortazavi, and G. Hibbard, "Characterization of Surface Defects on Pulse-Electrodeposited Nickel Tubes," Pract. Metallogr., 2013.

[107] M. Esmaily, N. Mortazavi, M. Shahabi-Navid, J. E. Svensson, L. G. Johansson, and M. Halvarsson, "On the capability of in-situ exposure in an environmental scanning electron microscope for investigating the atmospheric corrosion of magnesium," Ultramicrosco., vol. 153, pp. 45–54, 2015.

[108] C. Proff, S. Abolhassani, M. M. Dadras, and C. Lemaignan, "In situ oxidation of zirconium binary alloys by environmental SEM and analysis by AFM, FIB, and TEM," J. Nucl. Mater., vol. 404, no. 2, pp. 97–108, 2010.

[109] S. Abolhassani, M. Dadras, M. Leboeuf, and D. Gavillet, "In situ study of the oxidation of Zircaloy-4 by ESEM," J. Nucl. Mater., vol. 321, no. 1, pp. 70–77, 2003.

[110] T. Jonsson, N. Folkeson, J. E. Svensson, L. G. Johansson, and M. Halvarsson, "An ESEM in situ investigation of initial stages of the KCl induced high temperature corrosion of a Fe-2.25Cr-1Mo steel at 400°C," Corros. Sci., vol. 53, no. 6, pp. 2233–2246, 2011.

[111] T. Jonsson, B. Pujilaksono, S. Hallström, J. Ågren, J.-E. Svensson, L.-G. Johansson, and M. Halvarsson, "An ESEM in situ investigation of the influence of H_2O on iron oxidation at 500°C," Corros. Sci., vol. 51, no. 9, pp. 1914–1924, 2009.

[112] A. Deal, T. Hooghan, and A. Eades, "Energy-filtered electron backscatter diffraction," Ultramicrosco., vol. 108, no. 2, pp. 116–125, 2008.

[113] D. P. Field, "Improving the Spatial Resolution of EBSD," Microsc. Microanal., vol. 11, no. S02, pp. 52–53, 2005.

[114] V. G. M. Sivel, F. D. Tichelaar, H. Mohdadi, P. F. A. Alkemade, and H. W. Zandbergen, "Crystallographic analysis of thin specimens," J. Microsc., vol. 218, no. 2, pp. 115–124, 2005.

[115] R. H. Geiss, D. T. Read, G. B. Alers, and R. L. Graham, "EBSD analysis of narrow damascene copper lines," AIP Conf. Proc., vol. 1173, pp. 154–158, 2009.

[116] J. L. Sun, P. W. Trimby, F. K. Yan, X. Z. Liao, N. R. Tao, and J. T. Wang, "Grain size effect on deformation twinning propensity in ultrafine-grained hexagonal close-packed titanium," Scr. Mater., vol. 69, no. 5, pp. 428–431, 2013.

[117] J. L. Sun, P. W. Trimby, X. Si, X. Z. Liao, N. R. Tao, and J. T. Wang, "Nano twins in ultrafine-grained Ti processed by dynamic plastic deformation," Scr. Mater., vol. 68, no. 7, pp. 475–478, 2013.

[118] K. Tugcu, G. Sha, X. Z. Liao, P. Trimby, J. H. Xia, M. Y. Murashkin, Y. Xie, R. Z. Valiev, and S. P. Ringer, "Enhanced grain refinement of an Al-Mg-Si alloy by high-pressure torsion processing at 100°C," Mater. Sci. Eng. A, vol. 552, pp. 415–418, 2012.

[119] S. Birosca, R. Ding, S. Ooi, R. Buckingham, C. Coleman, and K. Dicks, "Nanostructure characterisation of flow-formed Cr–Mo–V steel using transmission Kikuchi diffraction technique," Ultramicrosco., vol. 153, pp. 1–8, 2015.

[120] K. Babinsky, W. Knabl, A. Lorich, R. De Kloe, H. Clemens, and S. Primig, "Grain boundary study of technically pure molybdenum by combining APT and TKD," Ultramicrosco., pp. 1–7, 2015.

[121] S. Suzuki, "Features of transmission EBSD and its application," Jom, vol. 65, no. 9, pp. 1254–1263, 2013.

[122] V. Bedekar, R. Shivpuri, A. Avishai, and R. S. Hyde, "Transmission Kikuchi Diffraction study of texture and orientation development in nanostructured hard turning layers," CIRP Ann. Manuf. Technol., vol. 64, no. 1, pp. 73–76, 2015.

[123] W. K. Yeoh, X. Y. Cui, B. Gault, K. S. B. De Silva, X. Xu, H. W. Liu, H.-W. Yen, D. Wong, P. Bao, D. J. Larson, I. Martin, W. X. Li, R. K. Zheng, X. L. Wang, S. X. Dou, and S. P. Ringer, "On the roles of graphene oxide doping for enhanced supercurrent in MgB$_2$ based superconductors.," Nanoscale, vol. 6, no. 11, pp. 6166–72, 2014.

[124] J. Hu, A. Garner, N. Ni, A. Gholinia, R. J. Nicholls, S. Lozano-Perez, P. Frankel, M. Preuss, and C. R. M. Grovenor, "Identifying suboxide grains at the metal–oxide interface of a corroded Zr–1.0%Nb alloy using (S)TEM, transmission-EBSD and EELS," Micron, vol. 69, pp. 35–42, 2015.

[125] K. Hellström, N. Israelsson, N. Mortazavi, S. Canovic, M. Halvarsson, J.-E. Svensson, and L.-G. Johansson, "Oxidation of a Dispersion-Strengthened Powder Metallurgical FeCrAl Alloy in the Presence of O2 at 1100 °C: The Influence of Water Vapour," Oxid. Met., vol. 83, no. 5–6, pp. 533–558, 2015.

[126] M. Meisnar, A. Vilalta-Clemente, A. Gholinia, M. Moody, A. J. Wilkinson, N. Huin, and S. Lozano-Perez, "Using transmission Kikuchi diffraction to study intergranular stress corrosion cracking in type 316 stainless steels," Micron, vol. 75, pp. 1–10, 2015.

[127] I. Utke, S. Moshkalev, and P. Russell, "Nanofabrication Using Focused Ion and Electron Beams: Principle and Applications," UK: OUP, 2012.

[128] W. Zhiming, "FIB Nanostructures, " Switzerland: Springer International Publishing, 2013.